Article

Cell

# Divergent Routes toward Wnt and R-spondin Niche Independency during Human Gastric Carcinogenesis

## Graphical Abstract

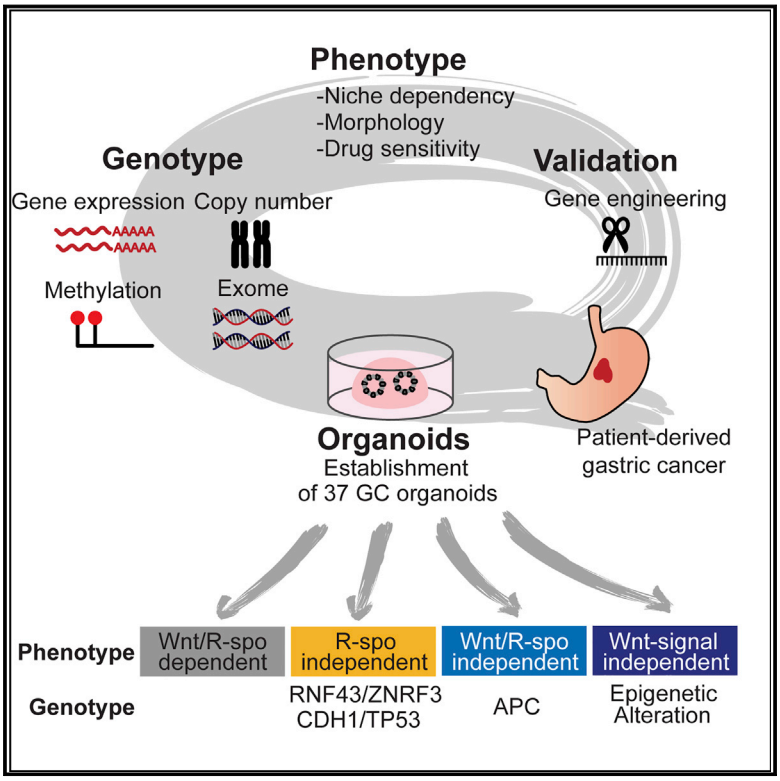


## Highlights

- Establishment of 37 patient-derived gastric cancer organoid lines
- Genotype-phenotype correlation analyses of gastric cancer organoids
- *CDH1/TP53* compound mutations confer R-spondin independency
- Wnt-targeting therapy is potent against a subset of human gastric cancers

## Authors

Kosaku Nanki, Kohta Toshimitsu, Ai Takano, ..., Bon-Kyoung Koo, Takanori Kanai, Toshiro Sato

## Correspondence

t.sato@keio.jp

## In Brief

Generation and analysis of a human gastric cancer organoid bank reveal insights into molecular features underlying diverse histopathological subtypes and tumor independence from Wnt signals.

Nanki et al., 2018, Cell *174*, 856–869
August 9, 2018 
https://doi.org/10.1016/j.cell.2018.07.027

CellPress

Cell

Article

# Divergent Routes toward Wnt and R-spondin Niche Independency during Human Gastric Carcinogenesis

Kosaku Nanki,[1,6] Kohta Toshimitsu,[1,6] Ai Takano,[1,6] Masayuki Fujii,[1] Mariko Shimokawa,[1] Yuki Ohta,[1] Mami Matano,[1] Takashi Seino,[1] Shingo Nishikori,[1,2] Keiko Ishikawa,[1] Kenta Kawasaki,[1] Kazuhiro Togasaki,[1] Sirirat Takahashi,[1] Yasutaka Sukawa,[1] Hiroki Ishida,[3] Shinya Sugimoto,[1] Hirofumi Kawakubo,[3] Jihoon Kim,[4] Yuko Kitagawa,[3] Shigeki Sekine,[5] Bon-Kyoung Koo,[4] Takanori Kanai,[1] and Toshiro Sato[1,7,*]

[1]Department of Gastroenterology, Keio University School of Medicine, Tokyo, 160-8582, Japan
[2]Fujii Memorial Research Institute, Otsuka Pharmaceutical Company, Limited, Shiga 520-0106, Japan
[3]Department of Surgery, Keio University School of Medicine, Tokyo, 160-8582, Japan
[4]Institute of Molecular Biotechnology of the Austrian Academy of Science, Vienna, 1030, Austria
[5]Division of Pathology and Clinical Laboratories, National Cancer Center Hospital, Tokyo, 104-0045, Japan
[6]These authors contributed equally
[7]Lead Contact
*Correspondence: t.sato@keio.jp
https://doi.org/10.1016/j.cell.2018.07.027

## SUMMARY

Recent sequencing analyses have shed light on heterogeneous patterns of genomic aberrations in human gastric cancers (GCs). To explore how individual genetic events translate into cancer phenotypes, we established a biological library consisting of genetically engineered gastric organoids carrying various GC mutations and 37 patient-derived organoid lines, including rare genomically stable GCs. Phenotype analyses of GC organoids revealed divergent genetic and epigenetic routes to gain Wnt and R-spondin niche independency. An unbiased phenotype-based genetic screening identified a significant association between *CDH1/TP53* compound mutations and the R-spondin independency that was functionally validated by CRISPR-based knockout. Xenografting of GC organoids further established the feasibility of Wnt-targeting therapy for Wnt-dependent GCs. Our results collectively demonstrate that multifaceted genetic abnormalities render human GCs independent of the stem cell niche and highlight the validity of the genotype-phenotype screening strategy in gaining deeper understanding of human cancers.

## INTRODUCTION

Gastric cancer (GC) is the fifth most common cancer and the third leading cause of cancer mortality worldwide (Torre et al., 2015). It is a highly heterogeneous disease presenting a range of histopathological appearances and molecular signatures. The Lauren classification has traditionally categorized GCs into two major histological subtypes: intestinal type GC (IGC) and diffuse type GC (DGC) (Lauren, 1965). IGC is characterized by a glandular or papillary structure with various differentiation degrees and frequently arises from intestinal metaplasia (IM) in association with *Helicobacter pylori* infection (Bosman et al., 2010). DGC exhibits a discohesive tissue architecture and typically arises from a non-IM background. Around 10%–15% of GCs consist of carcinoma with mixed intestinal and diffuse features, referred to as the Mixed type, or other rare histological subtypes, such as hepatoid adenocarcinoma. Recently, deep sequencing analyses have stratified GCs into four genetic subtypes: Epstein-Barr virus (EBV)-positive, microsatellite instability (MSI), chromosomal instability (CIN), and genomically stable (GS) GCs (Cancer Genome Atlas Research Network, 2014). Most intestinal and diffuse histological subtypes of GCs fall into the CIN and GS subtypes, respectively, indicating the robust correlation between genetic and histological classifications. Genetic analyses additionally identified recurrent genetic mutations in each subtype, for instance, frequent *CDH1* and *RHOA* mutations in the GS subtype (Cancer Genome Atlas Research Network, 2014; Kakiuchi et al., 2014; Wang et al., 2014). Despite these clear views of the genetic diversity across human GCs, the mechanistic connection between their genotypes and phenotypes has largely remained unclear, owing to a lack of functionally tractable platforms for human GC research.

To date, numerous genetically engineered mice have been generated to model spontaneous gastric tumorigenesis *in vivo* (Hayakawa et al., 2013; Poh et al., 2016). Though mouse models have provided important insights into GC pathogenesis, their genetic backgrounds are mostly irrelevant to the human GC genetics. Moreover, tumorigenesis in these genetic models requires long latency, suggesting that multiple genetic alterations are essential for the development of full-blown cancers. GC cell lines have alternatively served as accessible pre-clinical models for GC drug development. Nonetheless, their low establishment efficiency and biological distinction from clinical cancers often biases the interpretation of their phenotypes. Patient-derived xenograft models offer complementary means for mitigating these challenges, but several obstacles, such as the modest establishment efficiency, low throughput, and genetic intractability, remain open issues (Wang et al., 2017).

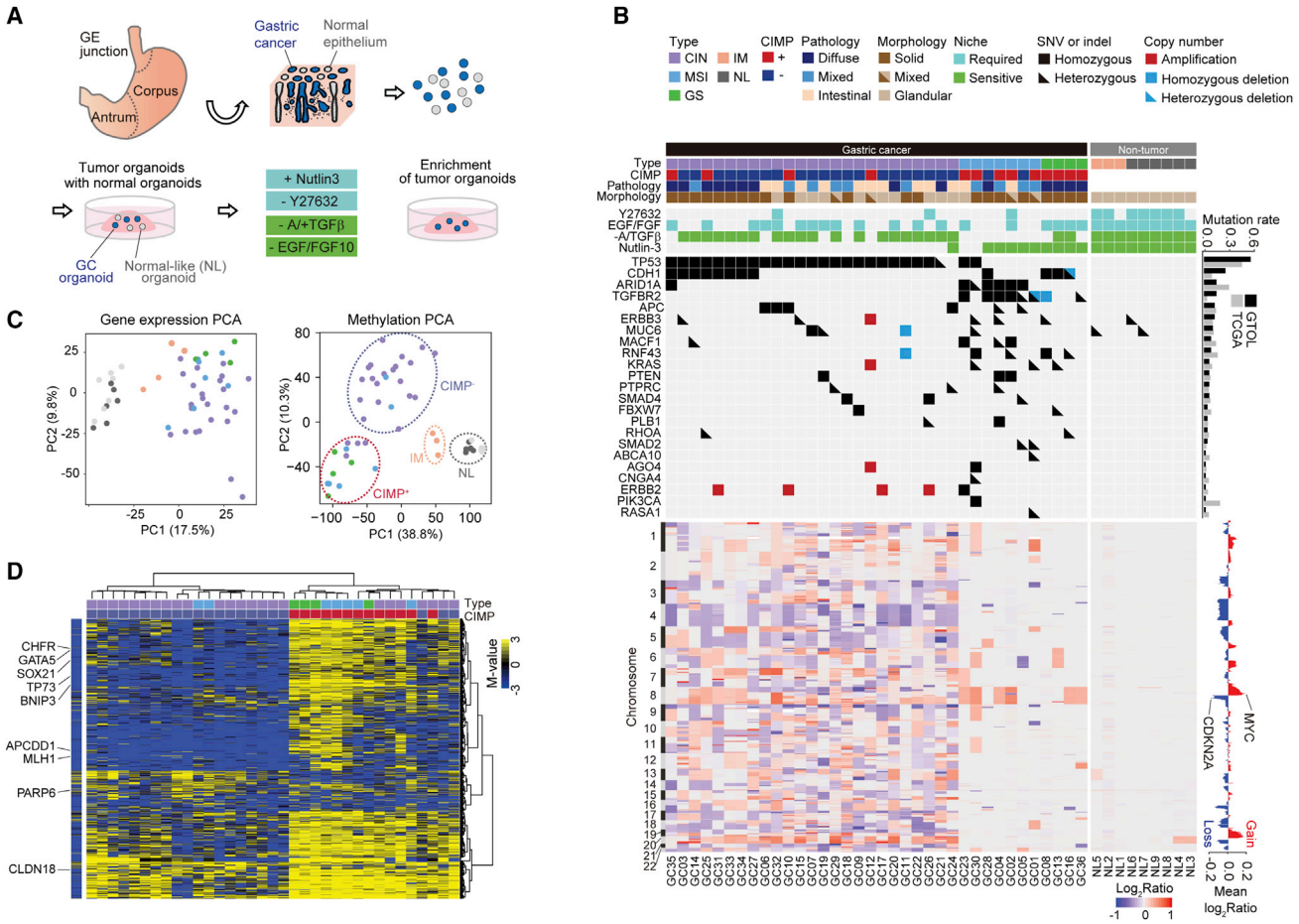


**Figure 1. Comprehensive Molecular Characterization of the GTOL**

(A) Establishment of GC organoids from clinical samples and the enrichment of cancer organoid by niche factor-based selections.

(B) Molecular (type/CIMP) and histological (pathology/morphology) subtypes, niche factor dependencies, genetic alterations and copy number statuses of the GTOL. Frequency of each genetic alteration in the GTOL and the TCGA report, and the overall copy number status across the GTOL is shown on the right.

(C) PCA plots for the transcriptome (left) and methylome (right). Each organoid is colored according to its type in (B). Normal organoids; light gray. CIMP statuses are indicated with dotted circles (right).

(D) Hierarchical clustering based on the methylation levels of top 1000 genes with highest variances in GC organoids. Average M-values in normal gastric organoids are shown on the left. Type and CIMP status colors are the same as those used in (B).

See also Figure S1 and S2.

Recently, the organoid technology has emerged as an option for culturing patient-derived GCs, which allows long-term expansion of human gastric epithelium using a specific combination of stem cell "niche factors" that are essential for the self-renewal of gastric epithelial stem cells—namely, Wnt-3A and R-spondin (Wnt signal activators), EGF, FGF10, Noggin (a BMP inhibitor), and A83-01 (a TGF-β inhibitor) (Barker et al., 2010; Bartfeld et al., 2015). Based on this technology, we generated a collection of 37 patient-derived GC organoids that largely covered the histological and molecular diversity of clinical GCs. Patient-derived GC organoids displayed varying niche factor dependencies defined by genetic and non-genetic mechanisms. Integrated genotype-phenotype analyses using patient-derived and CRISPR-Cas9-engineered gastric organoids directly illustrated how genetic alterations translate into cancer phenotypes, such as histopathological transformation and R-spondin independency.

## RESULTS

### Establishment and Enrichment of GC Organoids

Using the culture condition modified for gastric tissue, we sought to establish GC organoids from clinical GC samples (Figure 1A). During preliminary studies, we frequently experienced the overgrowth of normal gastric organoids from GC specimens, which hampered the establishment of slow-growing GC organoids. To circumvent the unintended overgrowth of normal organoids, we harnessed recurrently dysregulated signals in human GCs: the TP53, RHO, TGF-β, and RAS-PI3K pathways (Cancer Genome Atlas Research Network, 2014). To eliminate potentially existing normal organoids and enrich GC organoids, we first used Nutlin-3, an MDM2 inhibitor, to select *TP53* mutant GC organoids (Matano et al., 2015). Sequencing analyses confirmed the existence of *TP53* mutations in Nutlin-3 resistant organoids

(Figure 1B). Second, because ROCK inhibition is essential for the recovery of individualized organoid cells, we challenged them in a ROCK inhibitor (Y-27632)-free medium to enrich RHO-dysregulated GCs. Third, we treated the organoids with TGF-β in the absence of A83-01 to select GC organoids insensitive to TGF-β stimulation. Last, we used an EGF and FGF10 (EF)-removed culture condition to select organoids with ligand-independent receptor tyrosine kinase (RTK) signal activation (Figure 1B). These positive selections allowed for efficient generation of GC organoids from various lesions (primary tumors, metastases, and carcinomatous ascites) and histologic types, including poorly differentiated adenocarcinoma, signet ring cell carcinoma, and hepatoid adenocarcinoma (Table S1). The gross organoid establishment efficiencies before and after the protocol standardization were 54.7% (23 lines from 42 specimens) and 74.6% (44 lines from 59 specimens), respectively. Non-neoplastic gastric organoids were established in parallel from the same patients. We also established six normal gastric organoids from *Helicobacter pylori*-free donors and one IM organoid from an endoscopically diagnosed IM lesion. All established organoids were confirmed for their propagation persisting for at least 3 months and stored in liquid nitrogen for on-demand usage as a gastric tumor organoid library (GTOL).

## Genomic Characterization of GC Organoids

As described above, primary GC organoid culture often appears as a mosaic of GC and normal organoids, and their tumor-origin should thus be evaluated closely. Accordingly, we performed whole-exome sequencing (WES) and copy number and MSI analyses on selected organoids and defined their cancer origin by the following criteria: the presence of recurrent driver gene mutations, the existence of aneuploidy, or the sign of solid morphology with a loss of apicobasal polarity. Among the 67 lines of organoids derived from GC tissues, 46 lines were subjected to further WES analysis, of which 37 lines were judged as GC organoids. The remaining nine lines did not fulfill any of above criteria and were considered non-cancer organoids that had overgrown from GC tissues, hereafter called normal-like (NL) organoids (Figure 1B). Of note, all GC organoids were either insensitive to Nutlin-3/TGF-β treatment or independent of Y-27632, corroborating the stringency of the aforementioned niche-based selection steps. The establishment rate of GC organoids did not differ among histopathological subtypes.

We subsequently determined the genetic subtypes of the 36 established GC organoids based on the recent comprehensive molecular classification. We failed to derive EBV-positive GC organoids due to their rarity in our cohort. MSI and copy number analyses identified 7, 25, and 4 organoids as MSI-, CIN-, and GS-GCs, respectively. The mutation frequencies of the representative genes were comparable to those in previous reports except for the incidences of *CDH1*, *PIK3CA*, and *ARID1A* mutations, which may reflect different composition of molecular subtypes in our cohort (Figure 1B). Three of the 25 CIN-GC organoids were subjected to secondary WES after additional 3–5 passages. Comparison with the initial WES data confirmed their genetic stability during the culture period (Figure S1A). Copy number analyses identified recurrent gene amplifications and losses in a similar fashion as the previous report (Cancer Genome Atlas Research Network, 2014) (Figures 1B and S1B). The amplifications of cyclin and cyclin-dependent kinase genes (*CCNE1*, *CCND1*, and *CDK6*) were mutually exclusive to the homozygous deletions of cell cycle inhibitors (*CDKN2A* and *CDKN2B*) in GC organoids (Figure S1C).

Consistent with the original report, all four GS-GC organoids derived from DGCs showed minimal chromosomal alterations. The pure tumor composition of organoids unveiled diverse *CDH1* gene alterations in GS-GCs (Figures S1D–S1F). GC13 carried biallelic mutations in the cadherin domain. GC16 had a focal deletion of one allele and a mutation in the consensus splicing sequence in the remaining allele, which had initially been overlooked by the conventional mutation identifier in our pipeline. GC08 showed a single missense mutation accompanied by a copy-neutral loss of heterozygosity (CN-LOH) of the genomic region spanning *CDH1*. Of note, GC08 harbored *RNF43* and *TGFBR2* mutations, both of which involved CN-LOH (Figure S1G). These observations indicated that GS-GCs could accumulate functional genetic mutations through CN-LOH without any evident sign of aneuploidy. Indeed, copy number analysis identified an additional CN-LOH in the chromosome 20 of GC16 (Figure S1G). Although such precise genetic analyses of GS-GCs have been challenging owing to their low tumor purity, organoid-based cancer cell expansion enabled detection and characterization of minor genetic events occurring in GS-GC tissues.

## Transcriptomic Characterization of GC Organoids

We next investigated gene expression signatures of the GTOL using microarray analysis. Principal component analysis (PCA) largely separated GC organoids from normal and NL organoids, reinforcing the specificity of the criteria we used for diagnosing tumor origin (Figure 1C). Interestingly, the IM-derived organoid line and three NL organoids exhibited distinct gene expression patterns from those of normal gastric organoids. This population was characterized by the upregulation of the IM marker genes *CDX1*, *CDX2*, *VIL1*, *FABP1*, and *CDH17* and the downregulation of the gastric marker genes *SOX2*, *GKN1, GKN2*, and *KCNE2* (Melé et al., 2015) (Figure S2A). We confirmed the presence of IM in their original stomachs and thus included these NL organoids in IM organoids. IM organoids were morphologically indiscernible from normal gastric organoids, while immunostaining for CDX2 depicted the metaplastic change of IM organoids (Figure S2B).

We next performed methylation microarray analysis to gain insights into the diversified gene expression signatures of the GTOL. PCA clearly depicted normal, IM, and two subgroups within GC organoids, suggesting the presence of distinct epigenetic modifications in each population (Figure 1C). Different methylation patterns between IM and normal gastric organoids were consistent with a recent report on gastric tissues (Huang et al., 2018). The two methylation subtypes within GC organoids showed different methylation levels of gastric CpG island methylator phenotype (CIMP) genes (Wang et al., 2014), and we thus referred to these populations as $CIMP^{+}$ and $CIMP^{-}$ GCs (Figure 1D). Previous studies have associated most $MSI^{+}$ GCs with the CIMP, particularly with *MLH1* hypermethylation, which directs them toward the mutation-prone phenotype (Cancer Genome Atlas Research Network, 2014). Consistently, 5 of

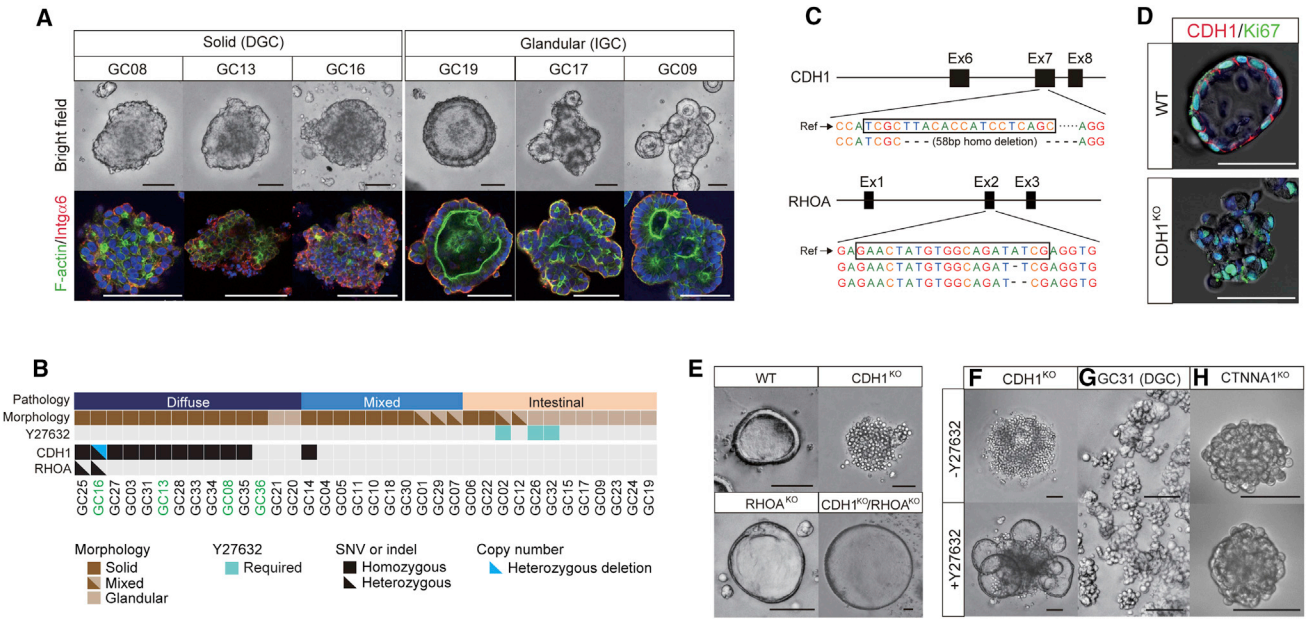


**Figure 2. Genetic Mutations Mediating Morphological Transformation of GC Organoids**

(A) Representative bright-field (top) and confocal (bottom) images of solid (left) and glandular organoid morphologies (right) with F-actin (green) and integrin-α6 (red) staining.

(B) Pathological and morphological subtypes, and Y-27632 requirement status of GC organoids, associated with *CDH1* and *RHOA* alterations. GS-GC organoids are highlighted in green characters.

(C) Sanger sequencing confirmation of *CDH1* and *RHOA* KO in single KO organoids. Black frames show sgRNA targets.

(D) CDH1 (red) and Ki67 (green) immunostaining validating *CDH1* KO and the viability of $CDH1^{KO}$ organoids, respectively.

(E) DGC-like morphological transformation by *CDH1* KO and the retention of the cystic structure by *RHOA* single-KO and *CDH1*/*RHOA* DKO.

(F–H) ROCK inhibitor (Y-27632) treatment on $CDH1^{KO}$ gastric organoids (F), DGC organoids (G) and $CTNNA1^{KO}$ gastric organoids (H). See also Video S1, a live-image of transforming $CDH1^{KO}$ organoid. Scale bar (A–H), 100 μm, nuclear counterstaining (A, D), Hoechst 33342.

See also Figure S3 and S4.

the 7 MSI-GC organoids showed $CIMP^+$ and *MLH1* hypermethylation, suggesting their persistent methylation patterns during culture. Of note, $CIMP^+$ and $CIMP^-$ GC organoids exhibited differing gene expression patterns (Figure S2C). The $CIMP^+$ GC-specific gene expression pattern extended to $CIMP^+$ colon tumor organoids when transcriptome data of gastric and colon tumor organoids were integrated (Figure S2D). These results highlight the common tumorigenic role of the CIMP in the gastrointestinal epithelium, consistent with the recent comprehensive molecular analysis on gastrointestinal cancers (Liu et al., 2018). The methylation analysis also assigned all four GS-GC organoids as $CIMP^+$ GCs. Unlike MSI-GC organoids, these GS-GC organoids were devoid of *MLH1* hypermethylation in line with their genetic stability. Although most GS-GCs have previously been categorized into the $CIMP^-$ subtype (Cancer Genome Atlas Research Network, 2014), massive infiltration of fibroblasts in GS-GC tissues might have biased their methylome data. In contrast, the organoid culture platform allowed the accurate determination of gene expression and DNA methylation patterns of GCs regardless of the tumor purity in original specimens.

## Morphological Characterization of GC Organoids

Established GC organoids exhibited various morphological appearances reminiscent of the diverse histological subtypes in clinical GCs. To connect the histological subtypes and the organoid structures, we classified GC organoids into "solid", "glandular", and "mixed" subtypes according to their morphological appearance (Figures 2A and S3). The solid subtype typically derived from DGCs and showed amorphous solid configurations with a loss of apicobasal polarity, while the glandular subtype was enriched with IGCs and typically formed single lumens lined by a single cellular layer. Analogous to the mixed histological GC subtype, we categorized cases comprising both solid and glandular populations into the mixed subtype. Our morphological subtypes largely matched their original histological subtypes, albeit with some inconsistencies (Figure 2B).

To investigate the stability of morphological phenotypes, we manually isolated solid and glandular organoids from parental mixed subtypes. These subcloned organoids retained their structures during culture, supporting their morphological stability (Figure S3). Of note, WES of mixed and glandular subclones from a mixed organoid line revealed a loss of genetic heterogeneity after the morphology-based subcloning, suggesting that the morphological diversification accrued along with the genetic heterogeneity formation (Figure S1A).

## Genetic Modeling of Morphological Transformation in DGCs

To gain insights into the mechanism of the morphological transformation during GC development, we determined the genetic

mutations responsible for the solid subtype in the GTOL. WES revealed recurrent *CDH1* mutations in solid GC organoids regardless of molecular subtypes, highlighting the role of *CDH1* mutations in specifying DGC-like organoid structures (Figure 2B). Two *CDH1* mutant DGC organoids simultaneously harbored *RHOA* mutations (one with G62E and the other with L22I). As was reported previously (Cancer Genome Atlas Research Network, 2014; Kakiuchi et al., 2014; Wang et al., 2014), both *RHOA* mutations in solid GC organoids were heterozygous and were found at recurrently mutated positions. To determine the functional effects of the *RHOA* mutations, we turned to a cell-line-based assay. An RHOA-fluorescence resonance energy transfer biosensor assay (Bindels et al., 2017) illustrated decreased affinity of $RHOA^{G62E}$ to the consensus RhoA-binding domain, which was suggestive of loss of function (Figures S4A and S4B).

To learn the phenotypic impact of *CDH1* and *RHOA* mutations in organoids, we next performed knockout (KO) of *CDH1* and/or *RHOA* genes in normal gastric organoids using CRISPR-Cas9 (Figures 2C and 2D). Both *CDH1* and *RHOA* single-KO organoids showed enhanced recovery from single cells without a ROCK inhibitor, consistent with their altered adhesion signaling pathway (Figure S4C). Nonetheless, without a ROCK inhibitor during passage, $CDH1^{KO}$ organoids diminished over time, whereas *CDH1*/*RHOA* double-KO (DKO) organoids vigorously propagated, suggesting that CDH1 loss alone was insufficient to abolish RHOA-ROCK-induced cell death induced by *anoikis* (Figure S4D). Addback induction of wild-type (WT) RHOA, but not $RHOA^{G62E}$, negated this $RHOA^{KO}$-mediated suppression of *anoikis*, reinforcing the observation that $RHOA^{G62E}$ had a loss-of-function impact (Figures S4E and S4F). Furthermore, the addback effect of $RHOA^{WT}$ was outcompeted when co-introduced with $RHOA^{G62E}$, indicating the dominant-negative effect of $RHOA^{G62E}$ (Figures S4F and S4G). While $RHOA^{KO}$ organoids maintained a normal cystic morphology, $CDH1^{KO}$ organoids showed a solid structure with a vigorous migratory activity (Figures 2D and 2E, Video S1). To our surprise, additional $RHOA^{KO}$ or ROCK inhibitor treatment of $CDH1^{KO}$ organoids reversed these phenotypes, indicating that morphological and migratory features of $CDH1^{KO}$ organoids require RHOA activation (Figure 2F, Video S1). In contrast to the response in $CDH1^{KO}$ normal gastric organoids, ROCK inhibitor treatment did not alter the solid structures of *CDH1* mutant DGC organoids (Figure 2G), underscoring the complex mechanisms regulating the morphological transformation.

CTNNA1 is an essential scaffolding molecule for adherens junctions that bridges the CDH1-CTNNB complex and the cytoskeleton (Takeichi, 2014). We noted that CTNNA1 expression was lost in $CDH1^{KO}$ organoids, whereas it reappeared after ROCK inhibitor treatment, suggesting the restoration of adherens junction during morphological reversion (Figure S4H). To determine the role of adherens junction in morphological transformation, we next knocked out *CTNNA1* in normal gastric organoids. *CTNNA1* is the only $\alpha$ catenin gene expressed in gastric organoids, and deletion of *CTNNA2* or *CTNNA3* did not induce morphological alteration (data not shown). In contrast, $CTNNA1^{KO}$ organoids recapitulated the solid structure of DGCs. Strikingly, the solid morphology of $CTNNA1^{KO}$ organoids was not reversed by ROCK inhibitor treatment, indicating that the disruption of adherens junctions was responsible for the solid structure phenotype (Figure 2H). Although somatic *CTNNA1* mutations are rather rare in sporadic GCs, germline *CTNNA1* mutations have been linked to the predisposition to familial DGC (Majewski et al., 2013). These data demonstrate that *CDH1* mutations destabilize the intercellular integrity of the glandular structure, but additional molecular defects are required to reinforce the morphological transformation in DGCs. Collectively, human GC modeling by genetic engineering of human gastric organoids provided insights into the histopathological transformation during human gastric tumorigenesis.

## EGF and FGF Niche-Dependent Growth Capacity in GC Organoids

To further investigate the genotype-phenotype correlations in GC, we next set our focus on the relationship between niche factor dependencies and genetic mutations (Figure 3A). GC organoids with a single *ERBB3* or *PTEN* mutation failed to grow in the absence of EF, suggesting that these mutations alone were insufficient for the acquisition of EF independency. One *KRAS*-mutant GC organoid (GC13) showed EF dependency despite the phosphorylation of downstream ERK in the absence of EF (Figures 3A–3C). Of note, $KRAS^{G12V}$ gastric organoids generated by CRISPR-Cas9-mediated mutation knockin could grow in an EF-free medium (Figure S5A), suggesting that GC13 organoids had negated the oncogenic impact of the *KRAS* mutation through an unknown mechanism.

In agreement with the preference for *ERBB* amplification in GCs, GC organoids with *ERBB2* or *ERBB3* amplification were invariably EF-independent. A pan-ERBB receptor kinase inhibitor (Ei) treatment abrogated the proliferation of four out of five *ERBB*-amplified organoids, indicating their cell-autonomous receptor hyperactivation (Figure 3B). The growth-inhibitory effect of Ei on gastric organoids was reversed by supplementation with another RTK ligand, HGF, excluding a toxic effect of Ei (Figure S5B). The auto-activation of downstream ERK in *ERBB*-amplified GC organoids was further confirmed by immunoassay (Figure 3C). Five GC organoids without genetic alterations in EGFR and FGFR signaling pathways were also independent of EF and sensitive to Ei. Because the cell-autonomous activation of EGFR family members is the only mechanism that can account for this phenotype, we reasoned that the gene expression of EGF-related molecules was altered in these organoids. Accordingly, transcriptome data showed upregulation of *EREG* (epiregulin), a ligand of EGFR, in three of five EF independent GC organoids (Figure 3D). Epiregulin substituted EF in normal gastric organoids (Figure S5B), suggesting that self-secretion of epiregulin contributed to EF independency.

Eight GC organoids tolerated Ei treatment. Three lines harbored genetic amplifications or mutations in *KRAS* and *PIK3CA*, which were presumed to drive this phenotype. In addition, three lines had genetic amplification of *FGFR2* or *MET*, which alternatively conferred Ei resistance on GC organoids (Figure 3A). Importantly, *MET*-amplified GC organoids were sensitive to a MET inhibitor, crizotinib (Figure 3E). These results indicate that the gastric epithelium engage multiple RTKs to efficiently activate RAS-PI3K pathways. Of note, two Ei-resistant

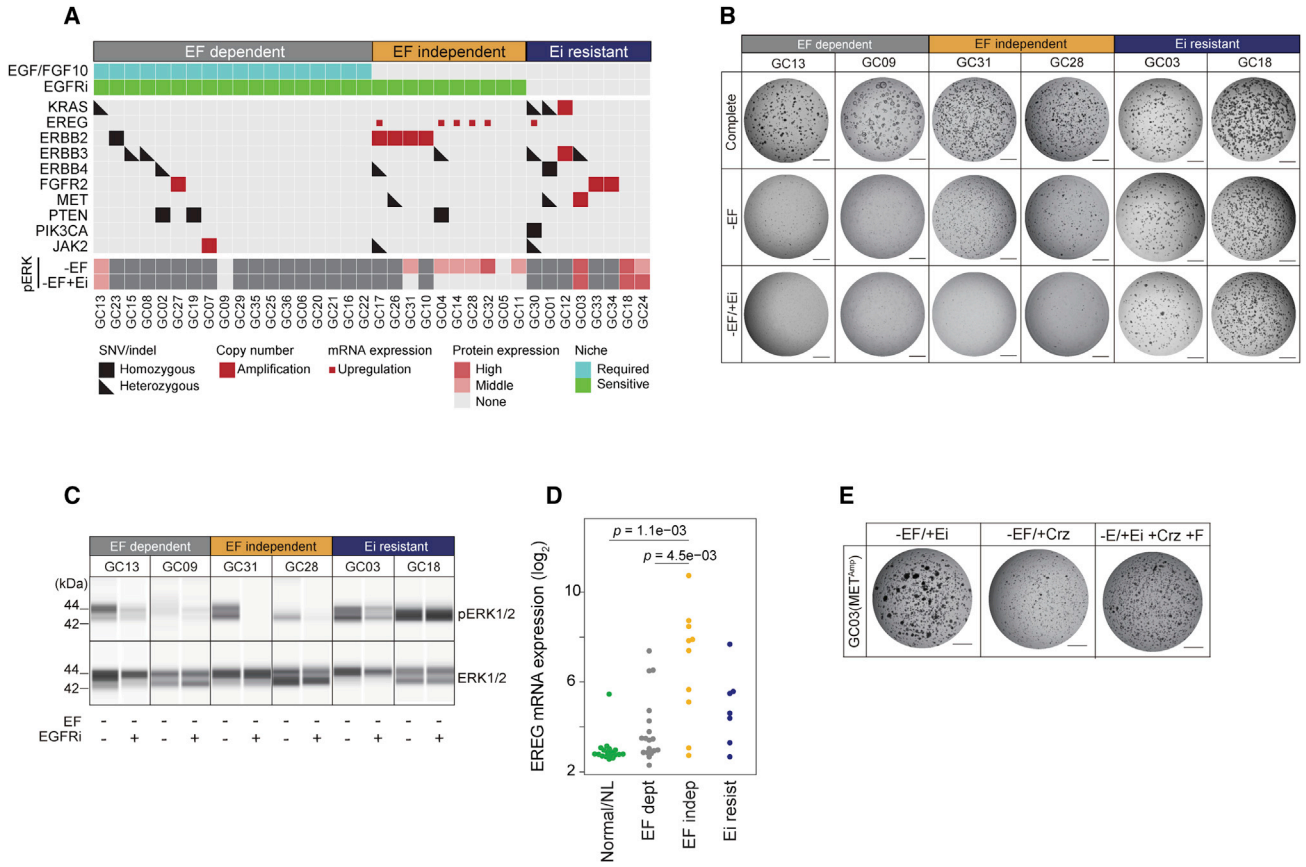


**Figure 3. Genetic Alterations Regulating EGF and FGF10 Niche Dependency**

(A) EGF/FGF10 (EF) dependency, EGFRi (Ei) sensitivity, associated with RTK pathway-related genetic alterations of GC organoids.

(B) Growth of EF-dependent, EF-independent and Ei-resistant GC organoids under EF-including (top), EF-removed (middle), and EF-removed/Ei-added conditions (bottom).

(C) Capillary-based immunoassays of phospho- and total ERK for the three types.

(D) *EREG* mRNA expressions in EGF niche subtypes. Each dot represents one organoid line. p value: Welch's t test.

(E) *MET*-amplified GC organoids (GC03) treated with Ei (left) or crizotinib (middle). FGF10 rescues growth inhibition by crizotinib (right). Scale bar, 1 mm.

See also Figure S5.

GC organoids were devoid of known genetic alterations that confer Ei resistance. Given the observations that niche-independent phenotypes are not necessarily determined *a priori* by genetic alterations in GCs, testing for Ei sensitivity in patient-derived GC organoids may be instructive when considering the indications for the ERBB pathway-targeting therapy, which is currently the standard of care for patients with ERBB2- positive GCs.

## BMP- and TGF-β-Resistant Phenotypes in GC Organoids

The requirement for TGF-β and BMP4 inhibition for gastric organoid culture suggests growth suppressive roles of these ligands. Conversely, TGF-β and BMP4 treatments did not affect the growth of GC organoids with *TGFBR2* and *SMAD4* mutations, respectively, indicating that these mutations confer resistance to TGF-β and BMP ligands (Figures S5C–S5E). In addition to these mutation-driven resistances, we noted that some GC organoids devoid of *TGFBR2* and *SMAD4* mutations also tolerated stimulation with TGF-β and BMP4 (Figure S5C). These results suggest that in human GCs, both genetic mutations and non-genetic mechanisms contribute to the tolerance against TGFβ and BMP-rich conditions and subsequently to the selective growth advantage in such environments, as was the case in colorectal cancers (Fujii et al., 2016).

## Wnt Niche-Independent Growth Capacity in GC Organoids

Wnt and R-spondin (WR) are indispensable for normal gastric epithelium organoids, but it remains unknown whether GCs acquire Wnt signal independency during their progression. In the GTOL, 16 GC organoids grew without exogenous Wnt-3A, of which 4 GC organoids were sensitive to a Porcupine inhibitor (Porcn-i; C59) (Figures 4A and 4B). Porcupine is essential for active Wnt ligand production (Proffitt et al., 2013) and thus these 4 GC organoid lines were considered dependent on endogenous Wnt production. In contrast, the other 12 GC organoids tolerated Porcn-i treatment and were judged to be Wnt ligand independent. Among these, six expressed *AXIN2*, a Wnt target gene,

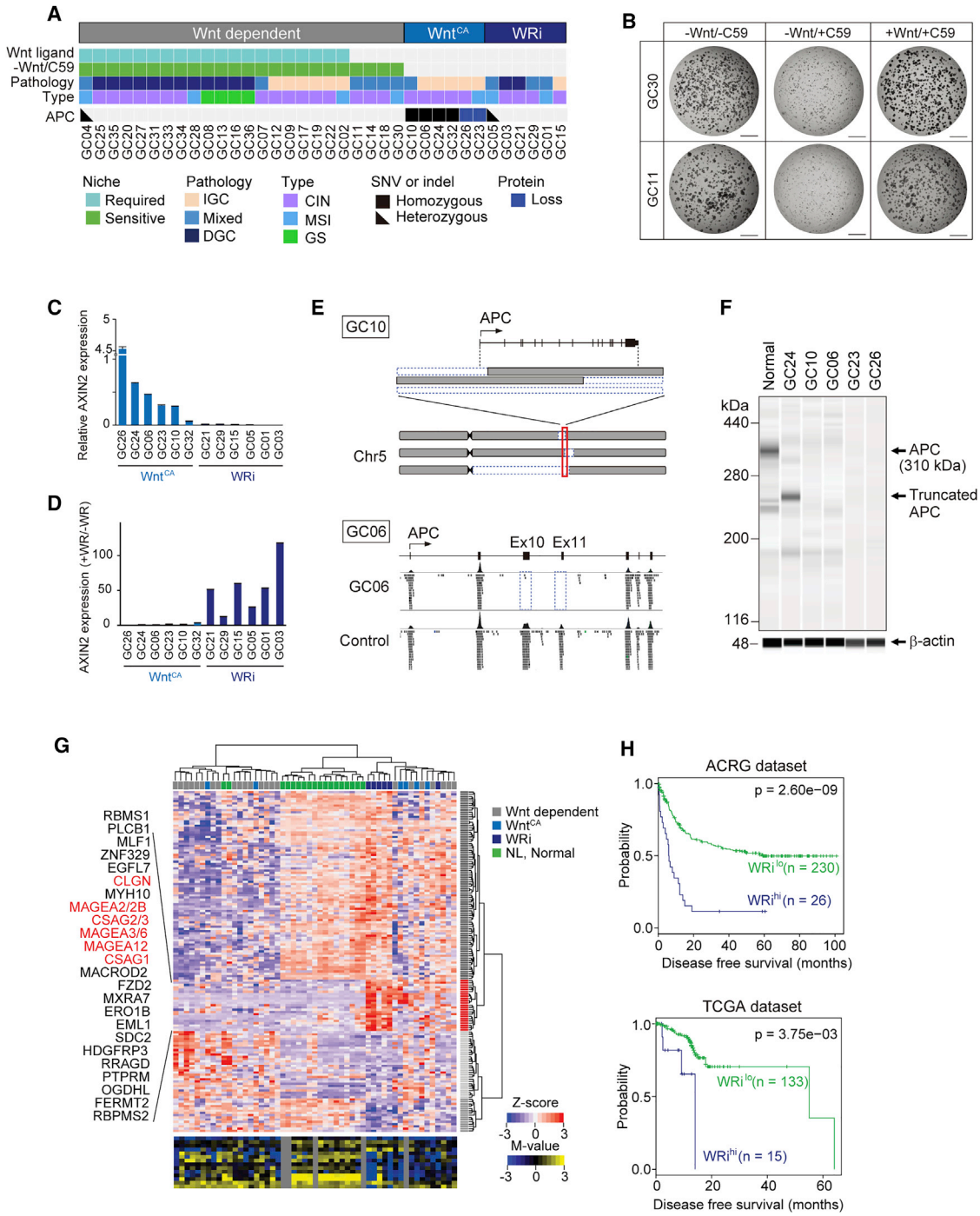


**Figure 4. Multiple Factors Specify Wnt Independency**

(A) Wnt ligand (Wnt-3A) requirements and Porcn-i (C59) sensitivity, associated with pathological subtypes, TCGA subtypes and *APC* gene alterations.

(B) Wnt-dependent organoids treated without (left) or with Porcn-i (C59) (middle) and the rescue by Wnt-3A (right). Scale bar, 1 mm.

(C) qPCR analysis of *AXIN2* expression in $Wnt^{CA}$ and WRi GC organoids cultured without WR. Data are shown as relative expression to *ACTB*.

(D) *AXIN2* expression ratio of WRi GC organoids cultured with versus without WR. Data are presented as the mean ± SEM (C, D).

(E) *APC* deletions in $Wnt^{CA}$ GC organoids. Complex chromosomal region spanning *APC* (GC10, top) and a biallelic focal deletion detected by missing WES reads in exon 10 and 11 (GC06, bottom).

(F) Capillary-based immunoassay for APC. Normal: normal gastric organoids.

(G) Unsupervised clustering of differentially expressed genes between WRi and other GC organoids. A cluster of genes specifically upregulated in WRi GC organoids (WRi genes) is highlighted, including cancer-testis genes (red). Methylation M-values of cancer-testis genes are shown below.

(H) Disease-free survival of GC patients stratified by the expression of WRi genes in the ACRG (top) and TCGA (bottom) cohorts. p value: log-rank test.

independently of WR, indicating constitutively active Wnt signaling ($Wnt^{CA}$) (Figures 4C and 4D). Within $Wnt^{CA}$ GC organoids, 4 lines harbored biallelic *APC* mutations or deletions (Figure 4E). Although we could not detect *APC* genetic alterations in the other two $Wnt^{CA}$ GC organoids, capillary-based immunoassay revealed APC protein loss (Figure 4F). These results demonstrate that GCs adopt diverse mechanisms to deactivate APC and acquire a $Wnt^{CA}$ phenotype.

The other 6 Wnt ligand-independent GC organoids showed intact ligand-induced Wnt pathway activation (Figure 4D), indicating that they were WR independent (WRi) despite the intact Wnt signaling. To characterize these WRi GC organoids, we next analyzed the transcriptomes of GC organoids. Hierarchical clustering identified a cluster of genes that were uniquely upregulated in WRi GC organoids, designated as the WRi genes (Figure 4G, Table S5). WRi genes included X-chromosome-linked cancer-testis genes, which exhibited extensive DNA demethylation. These results suggested the presence of epigenetic alterations that coaxed GCs toward the WRi phenotype. Of note, a previous report identified elevated expression and promoter demethylation of cancer-testis genes as a poor prognostic factor of GC (Honda et al., 2004). Furthermore, high expression level of WRi genes in GC was significantly associated with an unfavorable patient outcome in public GC transcriptome data (Figure 4H). These results collectively highlighted several mechanisms that render exogenous Wnt dispensable in GCs—namely, the self-secretion of Wnt, *APC* mutations, and epigenetic WRi regulation.

## RNF43-Mediated R-spondin Niche Independency in GC Organoids

Among the 24 Wnt ligand-dependent GC organoids, 15 GC organoids exhibited a unique R-spondin independency (Ri) (Figures 5A–5C). R-spondin binds to LGR4/5 and stabilizes the Wnt receptors, LRP and Frizzled; otherwise, these Wnt receptors are ubiquitinated by RNF43 and ZNRF3 (de Lau et al., 2011; Hao et al., 2012; Koo et al., 2012). Thus, the Ri phenotype could be attributed to two possible scenarios: auto-secretion of R-spondin by gene fusion and deletions of *RNF43* and *ZNRF3*. Because we did not detect an upregulation of R-spondin mRNAs in Ri GC organoids, the former mechanism was negated. The high frequency of *RNF43* mutations in GCs, identified in 15% of all cases (Wang et al., 2014), implied that the Ri phenotype might reflect defective RNF43. Consistently, *RNF43* mutations were enriched in Ri GC organoids (Figure 5A). As previously observed in intestinal organoids (Koo et al., 2012), *RNF43* single-KO gastric organoids remained dependent on R-spondin, underscoring the redundant function of an RNF43 homolog, ZNRF3 (data not shown). Our detailed genetic analyses further revealed various patterns of *RNF43* and *ZNRF3* gene alterations in Ri GC organoids. These genetic aberrations included not only RZ double mutations (Figure 5D) but also homozygous deletions of RZ (Figure 5E) and a concomitant mRNA downregulation of RZ (Figure 5F). Methylation microarray revealed CpG island methylation of *ZNRF3* in GC28.

Despite the importance of ZNRF3 loss for the Ri phenotype, two *RNF43* mutant Ri organoids lacked *ZNRF3* gene alterations (Figure 5A). These results prompted us to investigate whether single *RNF43* mutations could offer the Ri phenotype. One of these *RNF43* mutations (D300Y) was mapped onto its RING finger domain, suggesting a dominant-negative effect of this mutation (Figure 5G). To substantiate this possibility, we generated doxycycline-inducible expression constructs for $RNF43^{D300Y}$ and $RNF43^{WT}$ (Figure 5H). While the expression of $RNF43^{WT}$ did not affect the dependency on R-spondin (data not shown), $RNF43^{D300Y}$ expression conferred Ri on normal gastric organoids (Figure 5I), demonstrating that a specific *RNF43* mutation could alternatively induce Ri through a dominant-negative effect. One MSI-GC organoid harbored a heterozygous frameshift mutation in *RNF43* at a recurrently mutated site in MSI-GCs (G659fs) but remained strictly dependent on R-spondin (Figure 5B). Given our previous observation that MSI colorectal cancer organoids with the same mutation were also dependent on R-spondin (Fujii et al., 2016), this MSI-type *RNF43* mutation alone was considered insufficient for the Ri phenotype.

## Novel Genetic Mutations Rendering GC Organoids R-spondin Independent

Of 15 Ri GC organoids, 10 were devoid of *RNF43* alterations. To explore genetic mechanisms that confer Ri on RNF43-intact GC organoids, we conducted a phenotype-based mutation screening using the WES data of the GTOL. From recurrently mutated genes in WRd and Ri GC organoids and their combinations, an unbiased screening algorithm identified *CDH1* mutations and *CDH1*/*TP53* compound mutations as significantly enriched mutations in the Ri subtype versus the WRd subtype (Figure 6A). Consistently, seven of the 10 RNF43-intact Ri GC organoids harbored simultaneous *CDH1* and *TP53* mutations (Figure 6B). To investigate the causality between this genotype and the Ri phenotype, we generated *CDH1* and *TP53* single- or double-KO organoids from normal gastric organoids. Notably, either *CDH1* or *TP53* single-KO organoids remained dependent on R-spondin, whereas *CDH1*/*TP53* (CT)-DKO organoids gained an Ri phenotype (Figure 6C). CT DKO organoids were still dependent on exogenous Wnt-3A, suggesting that these organoids required Wnt signal activation (Figure 6D). The Ri phenotype by CT loss was validated using another line of normal gastric organoids (Figure S6A). We also generated CT-DKO organoids from two human IM organoid lines and one colon organoid line. Although CT-DKO IM and colon organoids acquired Nutlin-3 resistance and a discohesive morphology, they failed to grow in the absence of R-spondin (Figures 6C and S6A). These results suggested that CT loss induces Ri uniquely during gastric tumorigenesis.

To further characterize the CT loss-mediated Ri-phenotype, we analyzed the transcriptomes of CT-engineered organoids. *CDH1* single-KO in gastric organoids induced the expression of cell-cycle-inhibitor genes, including *CDKN2A*, *CDKN1A*, and *CDKN2B*, whereas this effect was not observed in CT-DKO gastric organoids. CT-DKO further showed higher expression of Wnt target genes as compared to normal and $CDH1^{KO}$ gastric organoids (Figure S6B). This trend was also observed in the comparison between CT-DKO gastric and colon organoids (Figures S6B and S6C). These results suggest that CT loss increased the sensitivity to Wnt ligands and that TP53 loss blocked the

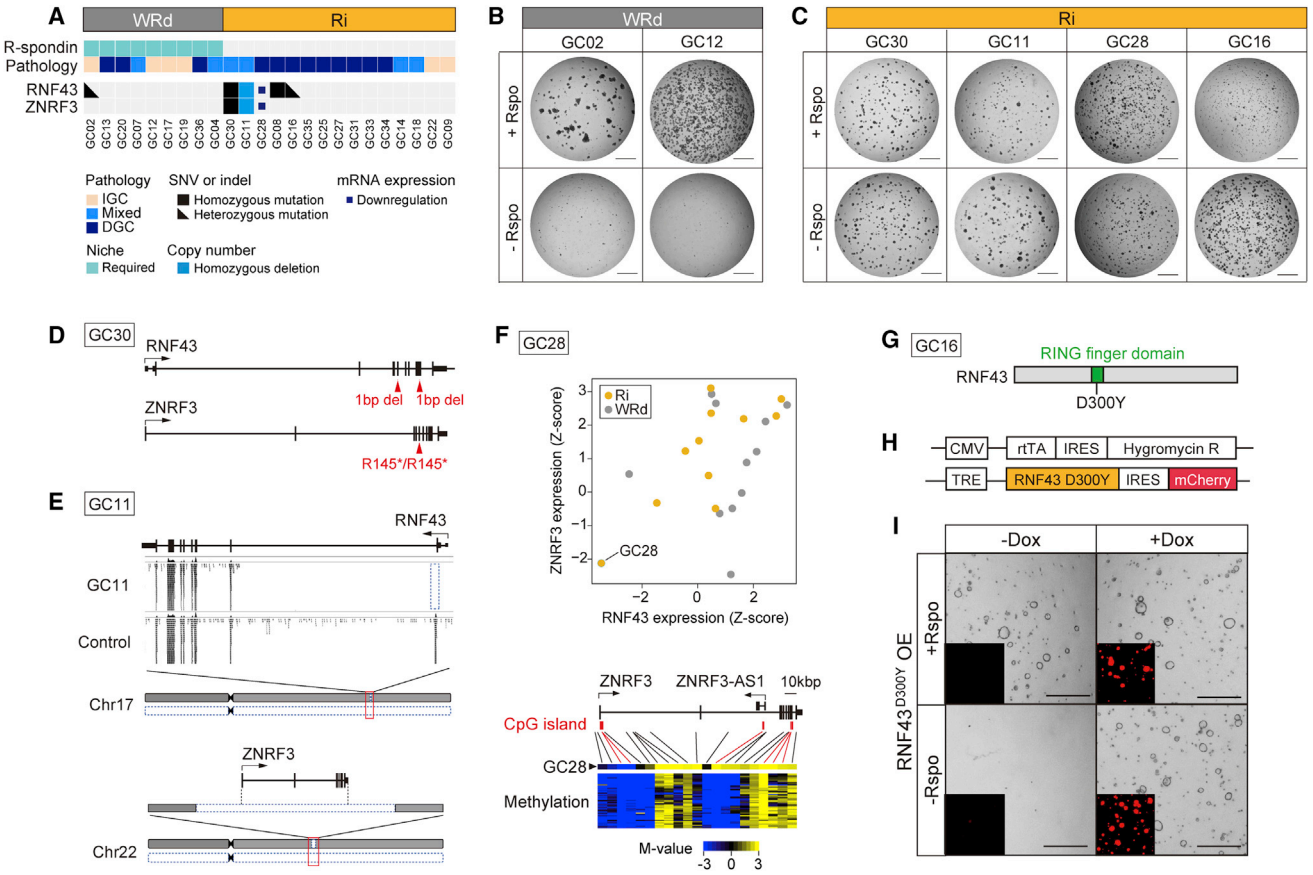


**Figure 5. *RNF43* and *ZNRF3* Alterations Regulate R-spondin Independency in GC Organoids**

(A) R-spondin dependency, associated with pathological subtypes and *RNF43*/*ZNRF3* gene alterations.

(B and C) WRd (B) and Ri (C) organoids cultured with (top) or without (bottom) R-spondin1.

(D and E) Somatic mutations (GC30, D) and deletions (GC11, E) in *RNF43* and *ZNRF3* in Ri GC organoids.

(F) *RNF43* and *ZNRF3* mRNA expressions in WRd and Ri GC organoids, with GC28 showing the lowest expression levels (top). GC11 with homozygous deletions of both genes are not shown. *ZNRF3* methylation status in GC28 and the remaining GC organoids (bottom). CpG islands are highlighted in red.

(G) The location of $RNF43^{D300Y}$ mutation.

(H) Constructs for doxycycline (Dox)-inducible $RNF43^{D300Y}$.

(I) Growth of Dox-inducible $RNF43^{D300Y}$ organoids in the indicated conditions. Insets show Dox-induced mCherry. Scale bar, 1 mm.

induction of cell cycle inhibitors by CDH1 loss. CT-DKO gastric organoids remained responsive to R-spondin in that they showed robust downregulation of Wnt target genes upon R-spondin withdrawal, indicating that CT loss confer an Ri phenotype despite the intact R-spondin-LGR4/5-RNF43/ZNRF3 axis (Figure S6D). In accordance with this result, RNF43 mutant GC organoids constitutively expressed Frizzled receptors regardless of R-spondin stimulation, while R-spondin removal decreased the surface expression levels of Frizzled receptors in WRd and CT mutant GC organoids (Figure 6E). These results collectively indicate that CT mutant GC organoids gain a unique Ri phenotype through a mechanism distinct from that of *RNF43*/*ZNRF3* mutations. Although the precise molecular mechanism remains to be determined, our results demonstrate that the organoid-based forward genetic approach enables the genetic interpretation of biological phenotypes of patient-derived cancers.

## *In Vivo* Testing of a Wnt-Targeting Therapy on Xenotransplanted Human GC Organoids

To generate preclinical *in vivo* models of human GCs, we attempted to establish a xenotransplantation system using GFP-labeled patient-derived GC organoids. When transplanted into kidney subcapsules of immunodeficient mice, only a fraction of GC organoids formed visible tumors. The particularly poor engraftment efficiency of WR-dependent GC organoids suggested the scarcity of the WR niche. Based on this notion, we co-transplanted GC organoids with human intestinal organoid-derived fibroblasts (HIOFs) that were generated from human pluripotent stem cells and known to produce WR (Watson et al., 2014) (Figure 7A). As we expected, co-transplantation with HIOFs significantly improved the engraftment efficiency of WR-dependent GC organoids (Figure 7B). Using this co-transplantation system, we established xenografts from 10 GC organoid lines. Importantly, the histopathological traits of parental tumors were

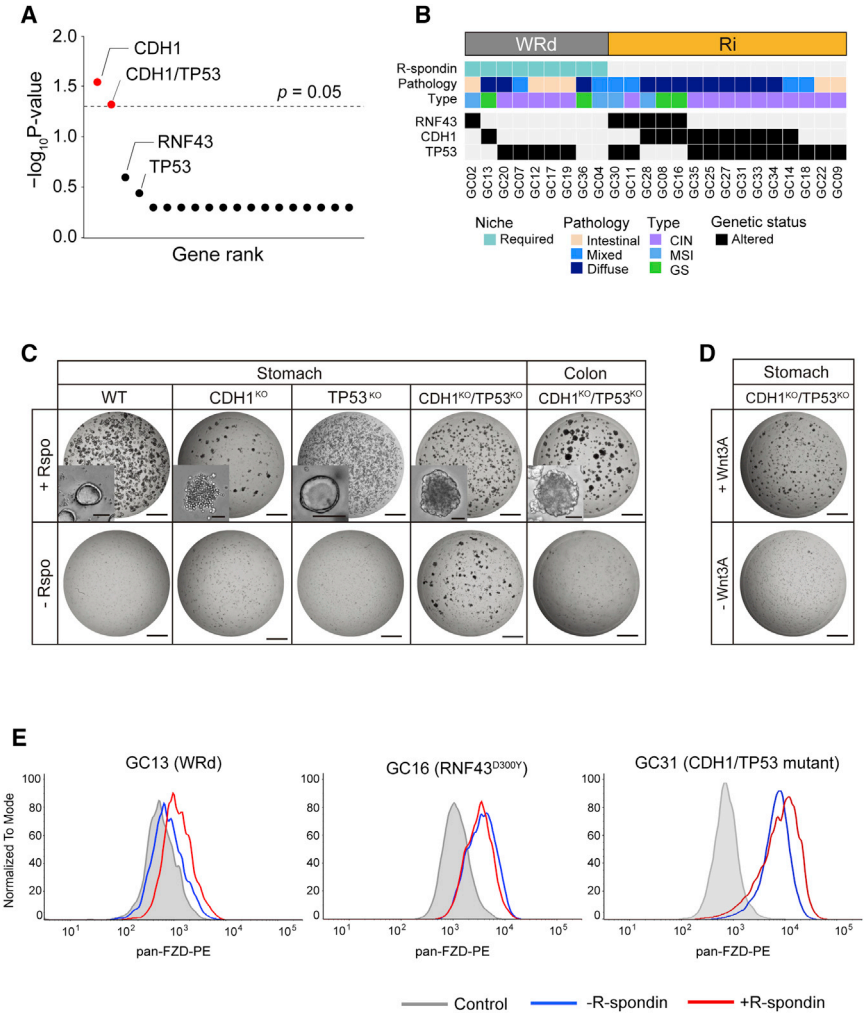


**Figure 6. *CDH1* and *TP53* Compound Mutations Are Responsible for R-spondin Independency in GC Organoids**

(A) Identification of mutated genes related to the Ri phenotype. Each dot represents the statictical significance of the gene and genes with p values of < 0.05 are shown in red.

(B) R-spondin dependency, associated with pathological and molecular subtypes, and indicated gene alterations.

(C) Growth of WT (parental normal), *CDH1*$^{KO}$, *TP53*$^{KO}$, *CDH1/TP53*-DKO gastric organoids, and CDH1/TP53-DKO colonic organoids with (top) or without R-spondin1 (bottom).

(D) Dependency of *CDH1/TP53*-DKO gastric organoids on Wnt-3A. Scale bar, 1 mm.

(E) Flow cytometry analysis of cell surface Frizzled expression with or without R-spondin. Frizzled expression is decreased by R-spondin withdrawal in WRd (left) and *CDH1/TP53*-mutated (right) but unaffected in *RNF43*$^{D300Y}$ -mutated GC organoids (middle).

See also Figure S6.

preserved in xenografts, indicating that histological subtypes were determined cell autonomously rather than by the surrounding niche environments (Figures 7C and S7A). GC organoids included various histological subtypes of GC, such as signet ring cell carcinoma, providing valuable opportunities for investigating rare GCs *in vivo*.

The high proportion of Wnt-dependent GCs in the GTOL inspired us to examine the feasibility of a Wnt-targeting strategy on human GCs by *in vivo* administration of a Porcn-i. To this end, we treated xenografts of three Ri, one Wnt$^{CA}$, and one WRi GC organoid with a Porcn-i (Figure 7D). Interestingly, Porcn-i treatment significantly reduced the tumor size of Ri GC grafts, but the therapeutic effect was not observed in Wnt$^{CA}$ and WRi GC organoids (Figures 7E and 7F). To validate that the Porcn-i specifically exerted this therapeutic effect through its Wnt-inhibitory function, we analyzed *AXIN2* expression in xenografts. As expected, Porcn-i treatment did not alter *AXIN2* expression in Wnt$^{CA}$ or WRi GC organoid tumors but significantly decreased its expression in Ri GC organoid grafts (Figures 7G and 7H). These results indicate that the niche-derived Wnt signal served as a vital lifeline for Ri GCs and that the Wnt niche could be a targetable module for a subset of Wnt-dependent human GCs.

## DISCUSSION

The pervasive histological and molecular heterogeneity across human GCs has hindered our access to the single patient-level connections between their genetic abnormalities and biological behaviors. To explore this relationship on an individualized basis, we generated a range of GC organoids that encompassed the histological, molecular, and phenotypic diversity of human GCs, including previously unestablished GS-GCs and hepatoid adenocarcinoma. The intensive characterization of GC organoids exposed novel associations between human GC genotypes and phenotypes, which were further cemented by prospective CRISPR engineering, xenotransplantation, and drug testing. Our GC organoid library not only provides a well-annotated resource for personalized human GC modeling and treatment, but it also highlights the power of the phenotype-based approach using patient-derived organoids in bridging the gap between the genetics and our current biological understandings of clinical GCs.

Of the four molecular subtypes of GC, the GS subtype has been considered the most ill-defined subgroup, both molecularly and functionally, owing to its low tumor purity and the lack of human cancer models. Capitalizing on the robustness of organoid technology, we successfully established four lines of GS-GC organoids characterized by DGC-like solid morphologies and minimal chromosomal alterations (Cancer Genome Atlas Research Network, 2014). GS-GC organoids exhibited chromosomal arm-level CN-LOHs encompassing known driver genes or fragile-site genes. In addition, all GS-GC organoids

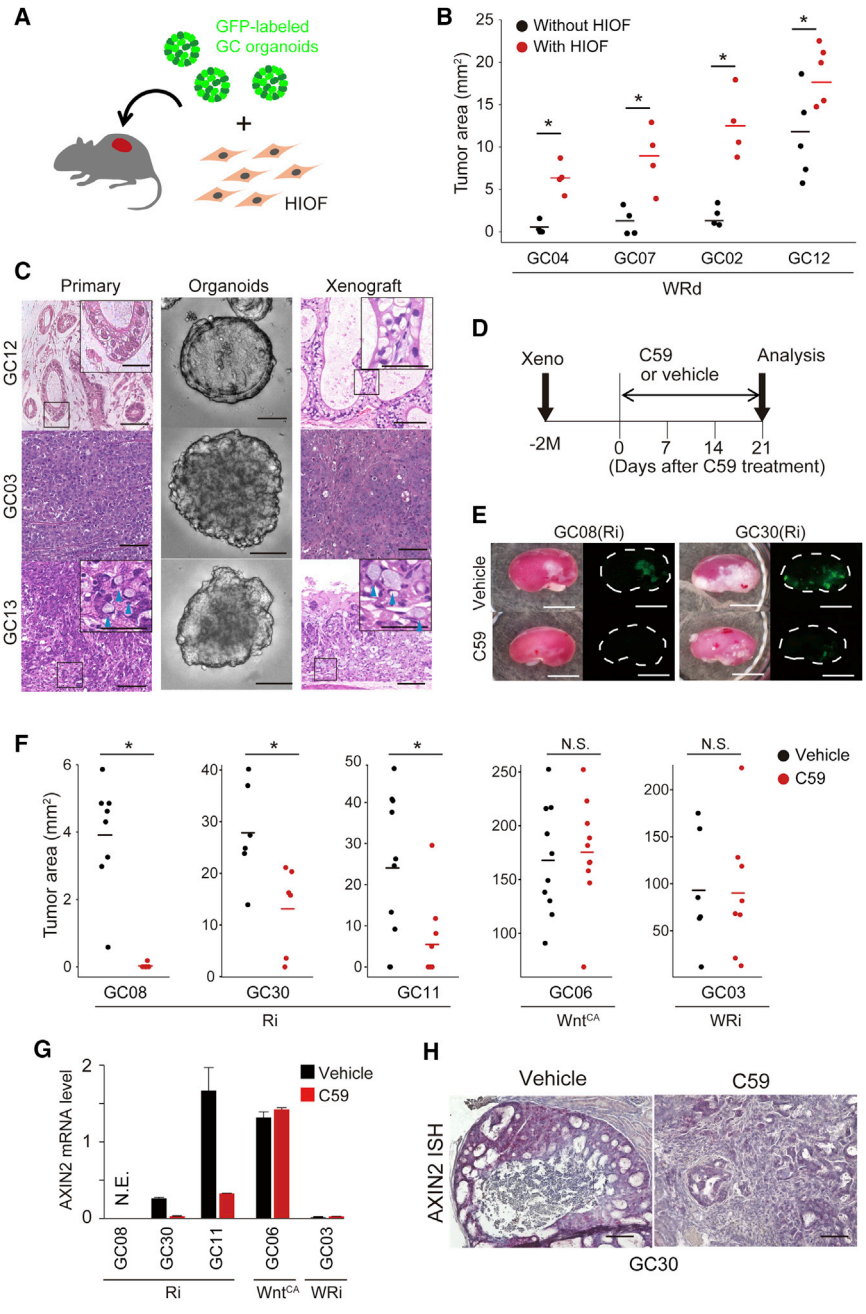


**Figure 7. *In Vivo* Analyses of Xenografted GC Organoids**

(A) A method for subrenal transplantation of GFP-labeled GC organoids with HIOF.

(B) Area of tumors transplanted alone (black) or with HIOFs (red). *p < 0.05, Welch's t test.

(C) Parental tumor histology (left), organoid morphology (middle) and xenograft histology (right) of well-differentiated adenocarcinoma (top), poorly differentiated adenocarcinoma (middle) and signet ring cell carcinoma organoids (bottom). Scale bar, 100 μm, 50 μm (insets). Blue arrowheads indicate signet-ring cells.

(D) C59 treatment schedule.

(E) Ri GC organoid xenografts, treated with vehicle (top) or C59 (bottom). Kidneys in fluorescent images are indicated by dotted circles. Scale bar, 5 mm.

(F) Tumor area of grafts treated with vehicle (black) or C59 (red). *p < 0.05, Welch's t test. N.S., not significant.

(G) qPCR analyses of *AXIN2* expression in GC xenografts treated with vehicle (black) or C59 (red). Relative expression to *ACTB* are shown. N.E., not examined due to tumor regression. Data are presented as the mean ± SEM.

(H) AXIN2 *in situ* hybridization of Ri GC xenografts treated with vehicle (left) or C59 (right). Scale bar, 100 μm.

See also Figure S7.

showed a CIMP-type methylation pattern, which has not been appreciated previously. These genetic and epigenetic modifications provided insights into the unique genetic basis of GS-GCs.

*RHOA* and *CDH1* mutations frequently co-occur in DGCs, yet their functional roles in human gastric tumorigenesis have remained elusive. In this study, we found that CRISPR-based *CDH1*$^{KO}$ organoids required inhibition of the RHOA-ROCK signal to sustain their growth as single cells, which might explain why these mutations preferentially co-occur. Recent literatures reported that *RHOA* mutations were not associated with the clinical progression of GCs (Röcken et al., 2016; Ushiku et al., 2016). Our result that ROCK inhibition deprived *CDH1*$^{KO}$ organoids of their mobility was compatible with these clinical findings and highlighted the ambivalent roles of RHOA mutations in gastric carcinogenesis. In contrast to *CDH1*$^{KO}$ organoids, *CDH1*-mutant DGC organoids maintained solid and mobile states regardless of ROCK inhibition. These results collectively suggested that molecular aberrations in addition to *CDH1* mutations are required to gain DGC characteristics represented by the morphological defect and the highly mobile phenotype.

We have previously proposed that the cancer driver gene mutations allow the stem cells to thrive independently of their native niche constraint (Date and Sato, 2015). Consistent with this notion, EGF, FGF10, epiregulin, and HGF were functional niche factors for gastric epithelial organoids, whereas the amplifications of RTK genes rendered the affected cells independent of these ligands. RTK-amplified or EREG-overexpressing GC organoids exhibited specific susceptibility to the corresponding RTK inhibitors, providing functional evidence for the effective genetics-based RTK targeting. Nonetheless, biological responses in GC organoids were not always genetically predictable. For example, *KRAS* mutations and *PTEN* mutations bypass ligand-dependent EGFR

activation in colorectal cancers (Fujii et al., 2016; Matano et al., 2015), but these mutations did not necessarily generate EF independency or Ei tolerability in GC organoids. In light of the recent co-clinical trial using patient-derived organoids (Vlachogiannis et al., 2018), we envision that organoid-based assays will provide more practical strategies for patient stratification toward personalized medicine.

R-spondin is one of the principal niche factors for gastrointestinal stem cells and its engagement with LGR5 counteracts RNF43 and ZNRF3 mediated degradation of Frizzled receptors. Consistent with previous studies on the intestinal epithelium (Koo et al., 2012; Schwank et al., 2013), concurrent RNF43 and ZNRF3 deletions were essential for the Ri phenotype in the human gastric epithelium. Nonetheless, previous genetic analyses rarely detected *ZNRF3* gene alterations (Cancer Genome Atlas Research Network, 2014; Kakiuchi et al., 2014; Wang et al., 2014). The existence of dominant-negative mutations in *RNF43* partially explained this discrepancy. Alternatively, homozygous deletions and CpG island methylations of *ZNRF3* induced Ri in cooperation with *RNF43* mutations. Therefore, despite the high prevalence of *RNF43* mutations, precise assessment of their biological impacts requires a thorough inspection of their mutational positions and the existence of concurrent *ZNRF3* gene alterations.

The GTOL comprised additional Ri GCs that were devoid of *RNF43* alterations. A forward-genetics approach revealed the enrichment of *CDH1/TP53* compound mutations in these *RNF43*-intact Ri GCs. Although both *CDH1* and *TP53* were considered independent cancer driver genes in GCs, our results suggest that these mutations could collaborate to gain a cancer phenotype. Interestingly, the functional synergy was tissue specific, as CT-DKO did not confer Ri on human IM or colon organoids. This result was consistent with previous findings that tissue-specific CT-DKO mice developed gastric but not intestinal cancers (Shimada et al., 2012; Park et al., 2014). Of note, CT-DKO mice also developed breast cancers (Derksen et al., 2006), and future studies may prove whether breast cancer organoids with CT mutations gain Ri. Unlike RZ mutant GC organoids, CT mutant organoids showed R-spondin-mediated Frizzled stabilization, suggesting that their Ri phenotype was driven by an RNF43-independent mechanism. Previous reports proposed that CDH1 loss activates Wnt signaling by unleashing membrane-bound β-catenin, which, in turn, activates Wnt/β-catenin signaling (Gottardi et al., 2001; Orsulic et al., 1999). Although CT-DKO organoids remained stringently dependent on exogenous Wnt-3A, they showed a higher level of Wnt signaling, suggesting that CT double loss imparted basal Wnt signaling activation which could render signal amplification by R-spondin dispensable. Further investigation is required to decipher the detailed molecular mechanisms of the CT mutation-mediated Ri phenotype.

Human GCs exhibited unique R-spondin independencies, while most of them remained dependent on Wnt ligands. This persistent dependency on Wnt ligands was a therapeutically actionable target for a subset of GCs. Using Porcn-i treatment, we demonstrated that Wnt targeting efficiently suppressed the tumorigenesis of Ri GCs. In contrast, Porcn-i treatment did not inhibit the growth of xenografts derived from WRi or $Wnt^{CA}$ GC organoids, which paralleled *in vitro* insensitivities to this compound. Clinical trials testing Porcn inhibitors for several types of cancers are currently underway (Lu et al., 2016). Because few effective molecular targeting strategies are available for DGCs, Wnt targeting in combination with organoid-based drug testing may open a new therapeutic avenue for patients with this fatal disease.

In summary, we established a patient-derived GC organoid library that encompasses various histological and genetic subtypes and offers a biological access to human GCs. By combining a phenotype-based screening and CRISPR-based reverse-genetics approach, we present a new paradigm for investigating the functional roles of driver gene mutations in GCs.

## STAR★METHODS

Detailed methods are provided in the online version of this paper and include the following:

- KEY RESOURCES TABLE
- CONTACT FOR REAGENT AND RESOURCE SHARING
- EXPERIMENTAL MODEL AND SUBJECT DETAILS
  - Generation of gastric normal and tumor organoids
  - Mice
- METHOD DETAILS
  - Gene manipulation of gastric organoids
  - RHOA activation assay using FRET biosensor
  - Time-Lapse Live Imaging
  - Molecular analyses for GC organoids
  - Genetic screening for the Ri phenotype
  - Gene Expression Microarray Analysis
  - Gene expression data analyses
  - Survival Analysis using Public Database
  - Real-Time Quantitative PCR
  - Capillary-based Immunoassay
  - Flow cytometry analysis
  - Xenografting of GC organoids
  - Immunohistochemistry and *in situ* hybridization
- QUANTIFICATION AND STATISTICAL ANALYSIS
- DATA AND SOFTWARE AVAILABILITY

## SUPPLEMENTAL INFORMATION

Supplemental Information includes seven figures, six tables, and one video and can be found with this article online at https://doi.org/10.1016/j.cell.2018.07.027.

## ACKNOWLEDGMENTS

This work was supported by AMED (Grant Numbers JP18cm0106206 and JP18gm5010002), by the JSPS KAKENHI (Grant Numbers JP17H06176, JP17K15967, and JP26115007). K. Toshimitsu., Y.O., and M.F. were supported by the Japan Society for the Promotion of Science Research Fellowships for Young Scientists. We also thank the Collaborative Research Resources, School of Medicine, Keio University for the technical assistance provided. HIO was a kind gift from J. Wells (Cincinnati Children's Hospital). We thank M. Takeichi (Riken BDR) for advice on CTNNA1.

## AUTHOR CONTRIBUTIONS

Conceptualization, K.N. and T. Sato; Methodology, K.N., K. Toshimitsu, A.T., Y.O., and T. Sato; Investigation, K.N., K. Toshimitsu, A.T., M.F., M.S., Y.O., M.M., T. Seino, S.N., K.I., K.K., K. Togasaki., S.T., Y.S., H.I., S. Sugimoto, and T. Sato; Data Curation, K. Toshimitsu, M.S., and Y.O.; Pathological assessment, S. Sekine; Writing, K.N., M.F., and T. Sato; Funding Acquisition, T. Sato; Resources, H.K., J.K., Y.K., B.-K.K., and T. K.

## DECLARATION OF INTERESTS

S.N. is an employee of Otsuka Pharmaceutical Company.

Received: March 23, 2018
Revised: June 29, 2018
Accepted: July 21, 2018
Published: August 9, 2018

## REFERENCES

Barker, N., Huch, M., Kujala, P., van de Wetering, M., Snippert, H.J., van Es, J.H., Sato, T., Stange, D.E., Begthel, H., van den Born, M., et al. (2010). Lgr5(+ve) stem cells drive self-renewal in the stomach and build long-lived gastric units in vitro. Cell Stem Cell *6*, 25–36.

Bartfeld, S., Bayram, T., van de Wetering, M., Huch, M., Begthel, H., Kujala, P., Vries, R., Peters, P.J., and Clevers, H. (2015). In Vitro expansion of human gastric epithelial stem cells and their responses to bacterial infection. Gastroenterology *148*, 126–136.

Bindels, D.S., Haarbosch, L., van Weeren, L., Postma, M., Wiese, K.E., Mastop, M., Aumonier, S., Gotthard, G., Royant, A., Hink, M.A., and Gadella, T.W., Jr. (2017). mScarlet: a bright monomeric red fluorescent protein for cellular imaging. Nat. Methods *14*, 53–56.

Bosman, F.T., Carneiro, F., Hruban, R.H., and Theise, N.D. (2010). WHO classification of tumours of the digestive system, 4th edn (Lyon: International Agency for Research on Cancer).

Brinkman, E.K., Chen, T., Amendola, M., and van Steensel, B. (2014). Easy quantitative assessment of genome editing by sequence trace decomposition. Nucleic Acids Res. *42*, e168.

Cancer Genome Atlas Research Network (2014). Comprehensive molecular characterization of gastric adenocarcinoma. Nature *513*, 202–209.

Cristescu, R., Lee, J., Nebozhyn, M., Kim, K.M., Ting, J.C., Wong, S.S., Liu, J., Yue, Y.G., Wang, J., Yu, K., et al. (2015). Molecular analysis of gastric cancer identifies subtypes associated with distinct clinical outcomes. Nat. Med. *21*, 449–456.

Date, S., and Sato, T. (2015). Mini-gut organoids: reconstitution of the stem cell niche. Annu. Rev. Cell Dev. Biol. *31*, 269–289.

de Lau, W., Barker, N., Low, T.Y., Koo, B.K., Li, V.S., Teunissen, H., Kujala, P., Haegebarth, A., Peters, P.J., van de Wetering, M., et al. (2011). Lgr5 homologues associate with Wnt receptors and mediate R-spondin signalling. Nature *476*, 293–297.

Derksen, P.W., Liu, X., Saridin, F., van der Gulden, H., Zevenhoven, J., Evers, B., van Beijnum, J.R., Griffioen, A.W., Vink, J., Krimpenfort, P., et al. (2006). Somatic inactivation of E-cadherin and p53 in mice leads to metastatic lobular mammary carcinoma through induction of anoikis resistance and angiogenesis. Cancer Cell *10*, 437–449.

Fujii, M., Matano, M., Nanki, K., and Sato, T. (2015). Efficient genetic engineering of human intestinal organoids using electroporation. Nat. Protoc. *10*, 1474–1485.

Fujii, M., Shimokawa, M., Date, S., Takano, A., Matano, M., Nanki, K., Ohta, Y., Toshimitsu, K., Nakazato, Y., Kawasaki, K., et al. (2016). A Colorectal Tumor Organoid Library Demonstrates Progressive Loss of Niche Factor Requirements during Tumorigenesis. Cell Stem Cell *18*, 827–838.

Gottardi, C.J., Wong, E., and Gumbiner, B.M. (2001). E-cadherin suppresses cellular transformation by inhibiting beta-catenin signaling in an adhesion-independent manner. J. Cell Biol. *153*, 1049–1060.

Hao, H.X., Xie, Y., Zhang, Y., Charlat, O., Oster, E., Avello, M., Lei, H., Mickanin, C., Liu, D., Ruffner, H., et al. (2012). ZNRF3 promotes Wnt receptor turnover in an R-spondin-sensitive manner. Nature *485*, 195–200.

Hayakawa, Y., Fox, J.G., Gonda, T., Worthley, D.L., Muthupalani, S., and Wang, T.C. (2013). Mouse models of gastric cancer. Cancers (Basel) *5*, 92–130.

Honda, T., Tamura, G., Waki, T., Kawata, S., Terashima, M., Nishizuka, S., and Motoyama, T. (2004). Demethylation of MAGE promoters during gastric cancer progression. Br. J. Cancer *90*, 838–843.

Huang, K.K., Ramnarayanan, K., Zhu, F., Srivastava, S., Xu, C., Tan, A.L.K., Lee, M., Tay, S., Das, K., Xing, M., et al. (2018). Genomic and Epigenomic Profiling of High-Risk Intestinal Metaplasia Reveals Molecular Determinants of Progression to Gastric Cancer. Cancer Cell *33*, 137–150 e135.

Kakiuchi, M., Nishizawa, T., Ueda, H., Gotoh, K., Tanaka, A., Hayashi, A., Yamamoto, S., Tatsuno, K., Katoh, H., Watanabe, Y., et al. (2014). Recurrent gain-of-function mutations of RHOA in diffuse-type gastric carcinoma. Nat. Genet. *46*, 583–587.

Koo, B.K., Spit, M., Jordens, I., Low, T.Y., Stange, D.E., van de Wetering, M., van Es, J.H., Mohammed, S., Heck, A.J., Maurice, M.M., and Clevers, H. (2012). Tumour suppressor RNF43 is a stem-cell E3 ligase that induces endocytosis of Wnt receptors. Nature *488*, 665–669.

Lauren, P. (1965). The Two Histological Main Types of Gastric Carcinoma: Diffuse and So-Called Intestinal-Type Carcinoma. An Attempt at a Histo-Clinical Classification. Acta Pathol. Microbiol. Scand. *64*, 31–49.

Liu, Y., Sethi, N.S., Hinoue, T., Schneider, B.G., Cherniack, A.D., Sanchez-Vega, F., Seoane, J.A., Farshidfar, F., Bowlby, R., Islam, M., et al. (2018). Comparative Molecular Analysis of Gastrointestinal Adenocarcinomas. Cancer Cell *33*, 721–735 e728.

Lu, B., Green, B.A., Farr, J.M., Lopes, F.C., and Van Raay, T.J. (2016). Wnt Drug Discovery: Weaving Through the Screens, Patents and Clinical Trials. Cancers (Basel) *8*. https://doi.org/10.3390/cancers8090082.

Majewski, I.J., Kluijt, I., Cats, A., Scerri, T.S., de Jong, D., Kluin, R.J., Hansford, S., Hogervorst, F.B., Bosma, A.J., Hofland, I., et al. (2013). An α-E-catenin (CTNNA1) mutation in hereditary diffuse gastric cancer. J. Pathol. *229*, 621–629.

Matano, M., Date, S., Shimokawa, M., Takano, A., Fujii, M., Ohta, Y., Watanabe, T., Kanai, T., and Sato, T. (2015). Modeling colorectal cancer using CRISPR-Cas9-mediated engineering of human intestinal organoids. Nat. Med. *21*, 256–262.

Melé, M., Ferreira, P.G., Reverter, F., DeLuca, D.S., Monlong, J., Sammeth, M., Young, T.R., Goldmann, J.M., Pervouchine, D.D., Sullivan, T.J., et al.; GTEx Consortium (2015). Human genomics. The human transcriptome across tissues and individuals. Science *348*, 660–665.

Mihara, E., Hirai, H., Yamamoto, H., Tamura-Kawakami, K., Matano, M., Kikuchi, A., Sato, T., and Takagi, J. (2016). Active and water-soluble form of lipidated Wnt protein is maintained by a serum glycoprotein afamin/α-albumin. eLife *5*, e11621.

Orsulic, S., Huber, O., Aberle, H., Arnold, S., and Kemler, R. (1999). E-cadherin binding prevents beta-catenin nuclear localization and beta-catenin/LEF-1-mediated transactivation. J. Cell Sci. *112*, 1237–1245.

Park, J.W., Jang, S.H., Park, D.M., Lim, N.J., Deng, C., Kim, D.Y., Green, J.E., and Kim, H.K. (2014). Cooperativity of E-cadherin and Smad4 loss to promote diffuse-type gastric adenocarcinoma and metastasis. Mol. Cancer Res. *12*, 1088–1099.

Poh, A.R., O'Donoghue, R.J., Ernst, M., and Putoczki, T.L. (2016). Mouse models for gastric cancer: Matching models to biological questions. J. Gastroenterol. Hepatol. *31*, 1257–1272.

Proffitt, K.D., Madan, B., Ke, Z., Pendharkar, V., Ding, L., Lee, M.A., Hannoush, R.N., and Virshup, D.M. (2013). Pharmacological inhibition of the Wnt

acyltransferase PORCN prevents growth of WNT-driven mammary cancer. Cancer Res. *73*, 502–507.

Randolph, L.N., Bao, X., Zhou, C., and Lian, X. (2017). An all-in-one, Tet-On 3G inducible PiggyBac system for human pluripotent stem cells and derivatives. Sci. Rep. *7*, 1549.

Röcken, C., Behrens, H.M., Böger, C., and Krüger, S. (2016). Clinicopathological characteristics of RHOA mutations in a Central European gastric cancer cohort. J. Clin. Pathol. *69*, 70–75.

Schwank, G., Koo, B.K., Sasselli, V., Dekkers, J.F., Heo, I., Demircan, T., Sasaki, N., Boymans, S., Cuppen, E., van der Ent, C.K., et al. (2013). Functional repair of CFTR by CRISPR/Cas9 in intestinal stem cell organoids of cystic fibrosis patients. Cell Stem Cell *13*, 653–658.

Seino, T., Kawasaki, S., Shimokawa, M., Tamagawa, H., Toshimitsu, K., Fujii, M., Ohta, Y., Matano, M., Nanki, K., Kawasaki, K., et al. (2018). Human Pancreatic Tumor Organoids Reveal Loss of Stem Cell Niche Factor Dependence during Disease Progression. Cell Stem Cell *22*, 454–467.

Shimada, S., Mimata, A., Sekine, M., Mogushi, K., Akiyama, Y., Fukamachi, H., Jonkers, J., Tanaka, H., Eishi, Y., and Yuasa, Y. (2012). Synergistic tumour suppressor activity of E-cadherin and p53 in a conditional mouse model for metastatic diffuse-type gastric cancer. Gut *61*, 344–353.

Sugimoto, S., Ohta, Y., Fujii, M., Matano, M., Shimokawa, M., Nanki, K., Date, S., Nishikori, S., Nakazato, Y., Nakamura, T., et al. (2018). Reconstruction of the Human Colon Epithelium In Vivo. Cell Stem Cell *22*, 171–176.

Takeichi, M. (2014). Dynamic contacts: rearranging adherens junctions to drive epithelial remodelling. Nat. Rev. Mol. Cell Biol. *15*, 397–410.

Torre, L.A., Bray, F., Siegel, R.L., Ferlay, J., Lortet-Tieulent, J., and Jemal, A. (2015). Global cancer statistics, 2012. CA Cancer J. Clin. *65*, 87–108.

Ushiku, T., Ishikawa, S., Kakiuchi, M., Tanaka, A., Katoh, H., Aburatani, H., Lauwers, G.Y., and Fukayama, M. (2016). RHOA mutation in diffuse-type gastric cancer: a comparative clinicopathology analysis of 87 cases. Gastric Cancer *19*, 403–411.

Vlachogiannis, G., Hedayat, S., Vatsiou, A., Jamin, Y., Fernández-Mateos, J., Khan, K., Lampis, A., Eason, K., Huntingford, I., Burke, R., et al. (2018). Patient-derived organoids model treatment response of metastatic gastrointestinal cancers. Science *359*, 920–926.

Wang, K., Yuen, S.T., Xu, J., Lee, S.P., Yan, H.H., Shi, S.T., Siu, H.C., Deng, S., Chu, K.M., Law, S., et al. (2014). Whole-genome sequencing and comprehensive molecular profiling identify new driver mutations in gastric cancer. Nat. Genet. *46*, 573–582.

Wang, H., Lu, J., Tang, J., Chen, S., He, K., Jiang, X., Jiang, W., and Teng, L. (2017). Establishment of patient-derived gastric cancer xenografts: a useful tool for preclinical evaluation of targeted therapies involving alterations in HER-2, MET and FGFR2 signaling pathways. BMC Cancer *17*, 191.

Watson, C.L., Mahe, M.M., Múnera, J., Howell, J.C., Sundaram, N., Poling, H.M., Schweitzer, J.I., Vallance, J.E., Mayhew, C.N., Sun, Y., et al. (2014). An in vivo model of human small intestine using pluripotent stem cells. Nat. Med. *20*, 1310–1314.

## STAR★METHODS

### KEY RESOURCES TABLE

| REAGENT or RESOURCE | SOURCE | IDENTIFIER |
|---|---|---|
| Antibodies | | |
| Rabbit monoclonal anti-Ki67 | Abcam | Cat#ab16667, RRID:AB_302459 |
| Rabbit polyclonal anti-p44/42 MAPK (Erk1/2) | Cell Signaling Technology | Cat#9102, RRID:AB_330744 |
| Rabbit monoclonal anti-phospho-p44/42 MAPK (Erk1/2) (Thr202/Tyr204) (D13.14.4E) | Cell Signaling Technology | Cat#4370, RRID:AB_2315112 |
| Rabbit monoclonal anti- RhoA (67B9) | Cell Signaling Technology | Cat#2117, RRID:AB_10693922 |
| Rabbit polyclonal anti-APC | Cell Signaling Technology | Cat#2504, RRID:AB_2057484 |
| OMP-18R5 (Human monoclonal anti-human Frizzled receptor) | Creative Biolabs | Cat#TAB-880, CAS; 1345009-45-1 |
| R-phycoerythrin Goat polyclonal anti-Human IgG, Fc fragment specific | Jackson Immune Reseach | Cat#109-115-098, RRID:AB_2337675 |
| Rat monoclonal anti-human/mouse CD49f (integrin α6) | Biolegend | Cat#313601, RRID:AB_345295 |
| Mouse monoclonal anti-β-actin | Sigma-Aldrich | Cat#A1978, RRID:AB_476692 |
| Mouse monoclonal anti-CDX2 | BioGenex | Cat#MU392, RRID:AB_2335627 |
| Goat polyclonal anti-E-cadherin | R&D | Cat#AF748, RRID:AB_355568 |
| Rabbit polyclonal anti-α-catenin | Sigma-Aldrich | Cat#C2081, RRID:AB_476830 |
| Phalloidin, Alexa Fluor 647 (F-actin) | Thermo Fisher Scientific | Cat#A22287, RRID:AB_2620155 |
| Donkey polyclonal anti-mouse IgG (H+L), Alexa Fluor 488 | Thermo Fisher Scientific | Cat#A-21202, RRID:AB_141607 |
| Goat polyclonal anti-rat IgG (H+L), Alexa Fluor 568 | Thermo Fisher Scientific | Cat#A-11077, RRID:AB_2534121 |
| Donkey polyclonal anti-goat IgG (H+L), Alexa Fluor 568 | Thermo Fisher Scientific | Cat#A-11057, RRID: AB_2534104 |
| Donkey polyclonal anti-rabbit IgG (H+L), Alexa Fluor 568 | Thermo Fisher Scientific | Cat#A10042, RRID:AB_2534017 |
| Donkey polyclonal anti-rabbit IgG (H+L), Alexa Fluor 647 | Thermo Fisher Scientific | Cat#A-31573, RRID:AB_2536183 |
| 20X anti-rabbit HRP conjugate | ProteinSimple | Cat#043-426 |
| Biological Samples | | |
| Human gastric tissue samples | This study | N/A |
| Human blood samples for sequence analyses | This study | N/A |
| Chemicals, Peptides, and Recombinant Proteins | | |
| Advanced DMEM/F12 | Thermo Fisher Scientific | Cat#12634010 |
| Human fibroblasts defined medium (HFDM-1) | Cell Science & Technology Institute | Cat#2102P05 |
| HEPES | Thermo Fisher Scientific | Cat#15630080 |
| Penicillin-Streptomycin | Thermo Fisher Scientific | Cat#15140122 |
| GlutaMAX Supplement | Thermo Fisher Scientific | Cat#35050061 |
| Matrigel | BD Biosciences | Cat#356231 |
| B-27 Supplement | Thermo Fisher Scientific | Cat#17504044 |
| N-Acetyl-L-cysteine | Sigma-Aldrich | Cat#A9165 |
| [Leu$^{15}$]-Gastrin I human | Sigma-Aldrich | Cat#G9145 |
| Afamin-Wnt-3A serum-free conditioned medium | Mihara et al., 2016 | N/A |
| Recombinant mouse EGF | Thermo Fisher Scientific | Cat#PMG8043 |
| Recombinant human R-spondin1 | R&D | Cat#4645-RS |
| Recombinant mouse Noggin | Peprotech | Cat#250-38 |
| Recombinant human FGF10 | Peprotech | Cat#100-26 |
| Recombinant human Epiregulin | Biolegend | Cat#550202 |
| Recombinant human HGF | Peprotech | Cat#100-39 |
| A83-01 | Tocris | Cat#2939 |

(*Continued on next page*)

*Continued*

| REAGENT or RESOURCE | SOURCE | IDENTIFIER |
|---|---|---|
| Recombinant human TGF-β1 | R&D | Cat#240-B |
| Y-27632 | Wako | Cat#253-00513 |
| EGFR/ErbB-2/ErbB-4 inhibitor | Merck Millipore | Cat#324840 |
| (±)-Nutlin-3 | Cayman Chemical | Cat#548472-68-0 |
| Recombinant human BMP4 | Peprotech | Cat#120-05ET |
| Wnt-C59 | ShangHai Biochempartner | Cat#1243243-89-1 |
| Recovery cell culture freezing medium | Thermo Fisher Scientific | Cat#12648010 |
| Crizotinib | Selleck Chemicals | Cat#S1068 |
| Fetal bovine serum | Biowest | Cat#S1820 |
| Liberase TH Research Grade | Roche | Cat#05401151001 |
| Cell Lysis Buffer | Cell Signaling Technology | Cat#9803 |
| Cell Recovery Solution | Corning | Cat#354253 |
| Cell Dissociation Buffer, enzyme-free, PBS | Thermo Fisher Scientific | Cat#13151014 |
| Hoechst 33342 | Thermo Fisher Scientific | Cat#H3570 |
| DAPI | BD Biosciences | Cat#564907 |
| SiR-Actin Kit | Cytoskeleton | Cat#CY-SC001 |
| TrypLE Express | Thermo Fisher Scientific | Cat#12605010 |
| Puromycin | Thermo Fisher Scientific | Cat#A1113802 |
| Blasticidin | Thermo Fisher Scientific | Cat#A1113903 |
| Hygromycin | InvivoGen | Cat#ant-hg |
| Doxycycline | Sigma-Aldrich | Cat#D9891 |
| BTXpress Solution | BTX | Cat#45-0805 |
| Opti-MEM I Reduced Serum Medium | Thermo Fisher Scientific | Cat#31985062 |
| Lipofectamin 2000 | Thermo Fisher Scientific | Cat#11668027 |
| RNase cocktail enzyme mix | Thermo Fisher Scientific | Cat#AM2286 |
| **Critical Commercial Assays** | | |
| RNAscope 2.5 HD Reagent Kit | Advanced Cell Diagnostics | Cat#322350 |
| QIAamp DNA Blood Mini Kit | QIAGEN | Cat#51106 |
| RNeasy Mini Kit | QIAGEN | Cat#74104 |
| Wes 12-230 kDa Master Kit | ProteinSimple | N/A |
| Wes 66-440 kDa Master Kit | ProteinSimple | N/A |
| Ominiscript RT kit | QIAGEN | Cat#205113 |
| Plasmid Plus Maxi Kit | QIAGEN | Cat#12965 |
| 12-230 kDa Wes Separation Module, capillary cartridges | ProteinSimple | Cat#SM-W004 |
| 66-440 kDa Wes Separation Module, capillary cartridges | ProteinSimple | Cat#SM-W008 |
| TOPO TA cloning Kit | Thermo Fisher Scientific | Cat#450641 |
| SureSelect XT Human All exon V5 | Agilent | Cat#5190-6209 |
| SureSelect XT Human All exon V6 | Agilent | Cat#5190-8864 |
| Cytoscan HD array | Thermo Fisher Scientific | Cat#901833 |
| Primeview human gene expression array | Thermo Fisher Scientific | Cat#901837 |
| RNeasy PLUS mini kit | QIAGEN | Cat#72134 |
| RNA6000 kit | Agilent | Cat#5067-1511 |
| FastStart Essential DNA Probes Master | Roche life science | Cat#06402682001 |
| Infinium MethylationEPIC BeadChip Kit | Illumina | Cat#WG-317-1001 |
| **Deposited Data** | | |
| Gene expression microarray of genetically engineered and 54 gastric organoids | This study | GEO: GSE112369 |
| Gene expression microarray of 58 colonic organoids | Fujii et al., 2016 | GEO: GSE74843 |

(*Continued on next page*)

*Continued*

| REAGENT or RESOURCE | SOURCE | IDENTIFIER |
|---|---|---|
| Gene expression microarray and clinical information of 300 primary gastric cancers deposited by ACRG | Cristescu et al., 2015 | GEO: GSE62254 |
| RNA-seq data and clinical information of 265 primary gastric cancers deposited by TCGA | Cancer Genome Atlas Research Network., 2014 | http://www.cbioportal.org/ |
| dbSNP | NIH | https://www.ncbi.nlm.nih.gov/snp/ |
| Human Genetic Variation Database | HGVD | http://www.hgvd.genome.med.kyoto-u.ac.jp/ |
| **Experimental Models: Cell Lines** | | |
| Human: gastric organoids: see Table S1 | This study | N/A |
| Human: colonic organoids | Sato Lab; Sugimoto et al., 2018 | N/A |
| Human: human intestinal organoids | Wells Lab; Watson et al., 2014 | N/A |
| **Experimental Models: Organisms/Strains** | | |
| Mouse: NOD.Cg-*Prkdc*$^{scid}$*Il2rg*$^{tm1Sug}$/Jic | Central Institute for Experimental Animals | N/A |
| **Oligonucleotides** | | |
| TP53 - gRNA | Matano et al., 2015 | gaatgaggccttggaactca |
| CDH1 - gRNA | This study | gctgaggatggtgtaagcga |
| RHOA - gRNA | This study | gaactatgtggcagatatcg |
| RNF43 - gRNA 1 | This study | aggggtccacacagttacga |
| RNF43 - gRNA 2 | This study | agtccgatgctgatgtaacc |
| CTNNA1 - gRNA | This study | gggccctctaataagaagag |
| CTNNA2 - gRNA | This study | ggaaatccggacgctaacag |
| CTNNA3 - gRNA | This study | aggagcccgagcttcactga |
| KRAS – gRNA | Matano et al., 2015 | gcatttttcttaagcgtcga |
| ACTB – qPCR forward primer | Seino et al., 2018 | ccaaccgcgagaagatga |
| ACTB – qPCR reverse primer | Seino et al., 2018 | ccagaggcgtacagggatag |
| ACTB – qPCR probe | Roche Universal Probe Library | #64 |
| AXIN2 – qPCR forward primer | Seino et al., 2018 | gctgacggatgattccatgt |
| AXIN2 – qPCR reverse primer | Seino et al., 2018 | actgcccacacgataaggag |
| AXIN2 – qPCR probe | Roche Universal Probe Library | #56 |
| RNAscope Probe Hs-AXIN2 | Advanced Cell Diagnostics | Cat#400241 |
| RNAscope Probe V-EBER1 | Advanced Cell Diagnostics | Cat#310271 |
| RNAscope Positive Control Probe Hs-PPIB | Advanced Cell Diagnostics | Cat#313901 |
| RNAscope Negative Control Probe DapB | Advanced Cell Diagnostics | Cat#310043 |
| **Recombinant DNA** | | |
| KRAS$^{G12V}$ donor vector | Matano et al., 2015 | N/A |
| XLone-GFP | Randolph et al., 2017 | Addgene Plasmid #96930 |
| pTriEx-RhoA-wt_mScarlet-i_SGFP2 | Bindels et al., 2017 | Addgene Plasmid #85071 |
| PiggyBac-CMV-MCS-EF1$\alpha$-GFP-T2A-Puro | System Biosciences | Cat#PB513B-1 |
| **Software and Algorithms** | | |
| R (version 3.4.3) | Comprehensive R Archive Network | https://cran.r-project.org/ |
| Affymetrix Power Tools (version 1.19.0) | Thermo Fisher Scientific | RRID:SCR_008401 |
| rCGH R package | R Bioconductor | https://bioconductor.org/packages/release/bioc/html/rCGH.html |
| GISTIC2.0 | Broad Institute | RRID:SCR_000151 |

(*Continued on next page*)

*Continued*

| REAGENT or RESOURCE | SOURCE | IDENTIFIER |
|---|---|---|
| wateRmelon R package | R Bioconductor | https://bioconductor.org/packages/release/bioc/html/wateRmelon.html |
| affy R package | R Bioconductor | https://bioconductor.org/packages/release/bioc/html/affy.html |
| sva R package | R Bioconductor | https://bioconductor.org/packages/release/bioc/html/sva.html |
| GSVA R package | R Bioconductor | https://bioconductor.org/packages/release/bioc/html/GSVA.html |
| Burrows-Wheeler Aligner (BWA) | Slashdot Media | RRID:SCR_010910 |
| Genome Analysis Toolkit (GATK) v. 1.6.13 | Broad Institute | RRID:SCR_006390 |
| Picard v.1.75 | Broad Institute | http://broadinstitute.github.io/picard/ |
| Samtools | Genome Research | RRID:SCR_002105 |
| Compass for SW | ProteinSimple | http://www.proteinsimple.com/compass/downloads/ |
| ImageJ | NIH | RRID:SCR_003070 |
| LAS X | Leica Microsystems | https://www.leica-microsystems.com/products/microscope-software/ |
| BZ-X analyzer | Keyence | N/A |
| LuminaVision | Mitani | https://www.mitani-visual.jp/download/catalogs/ |
| TIDE web tool | Netherlands Cancer Institute | https://tide.deskgen.com/ |
| SnpEff | Slashdot media | RRID:SCR_005191 |
| Other | | |
| TissueLyser LT | QIAGEN | Cat#85600 |

## CONTACT FOR REAGENT AND RESOURCE SHARING

Further information and requests for resources and reagents should be directed to and will be fulfilled by the Lead Contact, Toshiro Sato (t.sato@keio.jp).

## EXPERIMENTAL MODEL AND SUBJECT DETAILS

### Generation of gastric normal and tumor organoids

Clinical samples used for organoid establishment and biological analyses were obtained from patients at Keio University Hospital with informed consent after the approval of the ethical committee. Detailed clinical information is provided in Table S1. Healthy and GC specimens were collected by surgical resection, endoscopic biopsy, or ascites puncture. Organoids were established as previously reported (Bartfeld et al., 2015), with additional modifications for each GC sample type. Normal colon organoid line was previously established (Sugimoto et al., 2018). Surgical specimens were washed vigorously with phosphate-buffered saline (PBS) and minced into 1 $mm^3$ fragments using surgical scissors. The fragments were digested with Liberase TH (Roche) at 37°C for 30 min and undigested pellets were further treated with TrypLE Express (Thermo Fisher Scientific) at 37°C for 10 min. Prior to plating, collected epithelia were washed with PBS supplemented with 10% fetal bovine serum (FBS) to inactivate digestive enzymes. Ascites samples were centrifuged and washed 3 times with ice-cold PBS, and sedimented cells were used for organoid culture. Isolated gastric cells were embedded in Matrigel droplets and overlaid with the culture medium. The culture medium was prepared as previously described (Seino et al., 2018), except for addition of FGF10. Advanced Dulbecco's Modified Eagle's Medium/F12 was supplemented with penicillin/streptomycin, 10 mM HEPES, 2 mM GlutaMAX, 1 × B27 (Thermo Fisher Scientific), 10 nM gastrin I (Sigma), and 1 mM N-acetylcysteine (Wako, Japan) to prepare a basal culture medium. A complete medium was prepared by supplementing the basal culture medium with the following niche factors: 50 ng/ml mouse recombinant EGF (Thermo Fisher Scientific), 50 ng/ml human recombinant FGF10 (Peprotech), 100 ng/ml mouse recombinant noggin (Peprotech), 1 μg/ml human recombinant R-spondin1 (R&D), 25% Afamin-Wnt-3A serum-free conditioned medium (Mihara et al., 2016), and 500 nM A83-01 (Tocris). Plated organoids were maintained in a $CO_2$ incubator with 5% $CO_2$ and 20% $O_2$, and the media were changed every 3 or 4 days. For the enrichment of GC organoids, one-week treatment with 3 μM Nutlin-3 (Cayman Chemicals), culturing in the absence of Y-27632 (Wako) following complete single-cell dissociation, culturing in the absence of A83-01 and presence of TGF-β (10 ng/ml; R&D) and culturing in the absence of EGF and FGF10 were used. For the suppression of endogenous Wnt production, organoids were treated with 100 nM C59 (ShangHai Biochempartner). Once tumor-derived organoids were established, each niche factor was individually removed to

determine the minimally essential niche conditions. When the organoids survived without a given niche factor for at least 1 month, the organoids were judged as being independent of the niche factor. When the removal of a niche factor partially inhibited organoid growth, we extended the observation period to 3 months and judged the niche factor to be dispensable when the organoid was surviving and expandable at that point. Established organoids were subjected to molecular analyses and cryopreserved as previously described (Seino et al., 2018). For cryopreservation of the organoids, culture media was removed and added with 500 μl/well of recovery cell culture freezing medium (Thermo Fisher Sientific). Organoids and Matrigel were mechanically divided using 1,000 μL pipette and transfered into cryovials. Cryovials were placed into a freeze container, and incubated for 24 hr at −80°C. Frozen cryovials were then transferred to a liquid nitrogen storage tank.

### Mice

All animal procedures were approved by the Keio University School of Medicine Animal Care Committee. Male NOD/Shi-scid, IL-2Rγ null (NOG) mice were obtained from the Central Institute for Experimental Animals (CIEA, Japan) and housed under specific pathogen-free conditions.

## METHOD DETAILS

### Gene manipulation of gastric organoids

For gene knockout using CRISPR-Cas9, gene specific single-guide RNAs (sgRNAs) were cloned into the pX330-U6-Chimeric_BB-CBh-hSpCas9 vector. KI of *KRAS*$^{G12V}$ was performed as previously described (Matano et al., 2015) by co-introducing CRISPR vector into organoids with KRAS$^{G12V}$ donor vector. KO of *TP53*, *CDH1*, *RHOA, CTNNA1*, *CTNNA2*, *CTNNA3* and *RNF43* genes were performed by co-introducing each CRISPR vector into organoids with a GFP-puro expressing piggyBAC vector (PB513B-1, SBI), and organoids were subsequently treated with puromycin (2 μg/ml) to enrich organoids that have undergone successful plasmid delivery. *CDH1*, *RHOA* and *CTNNA1* mutants were further enriched by complete single cell dissociation of the organoids followed by the culture without Y-27632 as mentioned in the main text. *TP53* mutants were selected by 3 μM Nutlin-3. *KRAS*$^{G12V}$ mutants were selected by the EF-removed condition. As *CTNNA2*, *CTNNA3* and *RNF43* KO organoids could not be selected by culture conditions, puromycin-resistant single organoids were manually picked up. To obtain clonal KO organoids, single organoids were isolated and expanded. Successful gene KO by the introduction of biallelic frameshift mutations was confirmed by the TIDE (Brinkman et al., 2014) or Sanger sequencing using bacterially cloned DNA as previously described (Matano et al., 2015). Briefly, genomic DNA was extracted from engineered organoids, followed by PCR amplification of targeted loci. PCR products were directly analyzed, or cloned using TOPO-TA cloning kit (Thermo Fisher Scientific) and subsequently analyzed by Sanger sequencing. The results of the TIDE analyses are shown in Table S2.

For conditional-gene overexpression experiments, RHOA$^{WT}$ or RHOA$^{G62E}$ cDNA was cloned into the XLone-GFP vector (Randolph et al., 2017) (Addgene#96930) by replacing the GFP cassette using KpnI and SpeI digestion sites. For RHOA FRET activity analysis, RHOA$^{WT}$ or RHOA$^{G62E}$ cDNAs were fused to the C terminus of synthesized VN173 and linker peptides, and further attached to the N terminus of mScarlet-i fused with PKN1-RHO binding domain, which was then cloned into the XLone vector. Vectors were electrotransferred into organoids as previously described (Fujii et al., 2015) and were selected with blasticidin (5 μg/ml) in experiments using XLone vectors or with hygromycin (200 μg/ml) in experiments using the PB-Tet-on vector. Gene expression was induced using 50–500 ng/ml of Doxycycline.

### RHOA activation assay using FRET biosensor

To investigate the RHOA-GTP loading capacity of mutant RHOA$^{G62E}$, a doxycycline-inducible single chain FRET biosensor was synthesized based on a previously reported DORA-mScarlet-I-SGFP2 vector (Bindels et al., 2017). When RHOA-GDP is converted to RHOA-GTP, a PKN1 moiety binds to RHOA-GTP, resulting in a high FRET state, which is detected as an increase in sensitized emission over VN173 ratio. To examine the FRET ratio contrast between the active and inactive states, synthesized constitutively active Q63L mutant and primary inactivated T19N mutant RhoA were used as positive and negative controls, respectively. 293T cells were transfected with 4 μg of the plasmid, and were grown under general growth culture conditions for overnight, followed by a culture with doxycycline (50 ng/ml) in a serum-free medium for 16 hr. Sequential images (donor excitation-donor emission (Donor), donor excitation-acceptor emission (FRET), acceptor excitation-acceptor emission (Acceptor)) were recorded using a confocal microscope (SP8, Leica). The donor (VN173) was excited at 488 nm, and collected using a 493-593 nm filter. The acceptor (mScarlet-I) was excited at 562 nm, and emission was collected by a 576-676nm filter. In order to extract the pure donor or acceptor emission from sensitized emission, background intensities were determined from cells expressing donor only and acceptor only using the same microscope settings of the measurements. The drawing of the regions of interest on random transfected cells and raw intensity measurement were carried out automatically using the ImageJ. FRET ratios were obtained by calculating background-subtracted FRET intensities divided by background-subtracted donor intensities in each regions of interest.

### Time-Lapse Live Imaging

Time-lapse laser-scanning confocal fluorescence microscopy imaging of *CDH1*$^{KO}$ organoids was performed using the Confocal Quantitative Image Cytometer CQ1 (Yokogawa Electric). We used 50 nM SiR-actin (CY-SC001, Cytoskeleton), a fluorogenic F-actin

labeling chemical probe for live cells, for the visualization of F-actin. Cytoplasmic GFP was excited at 488 nm and collected using a 447/60 nm bandpass filter, and fluorophore silicon rhodamine-labeled F-actin was excited at 640 nm and collected using a 685/40 nm bandpass filter. After a Y-27632 wash out, z stack images were captured at 30-minute intervals for 3 days and reconstructed using the maximum-intensity projection method to make movies.

### Molecular analyses for GC organoids

DNA was extracted from organoids or blood with the QIAamp Blood Mini Kit (QIAGEN) and treated with RNase Cocktail (Ambion). The quality of DNA specimens was confirmed by agarose gel electrophoresis within the expected range of DNA fragmentation. Three micrograms of genomic DNA was fragmented for whole-exome sequencing analyses as previously described (Seino et al., 2018). Paired-end libraries were prepared using the SureSelect Human All Exon V5 or V6 kit (Agilent) according to the manufacturer's instructions and were sequenced using Illumina HiSeq2500 (outsourced to Hokkaido System Science) or HiSeq4000 (outsourced to BGI JAPAN K.K.). Cleaned fastq files were mapped onto human reference genome version GRCh37 (hg19) using BWA. The generated reads were processed with the Genome Analysis Toolkit (GATK, version 1.6.13). Single-nucleotide variations (SNVs), insertions, and deletions were detected using GATK UnifiedGenotyper. Variants were annotated using SnpEff and filtered by removing those registered in SNV databases (dbSNP build 130 or lower), in the 1000 Genomes Project with a frequency of $> 0.01$, or in the Japanese SNP database (the Human Genetic Variation Database). When pairwise normal organoids or blood samples were available, variants were further filtered by altering their allele frequency ($> 0.08$). Additionally, we confirmed the variants and indels as SNPs that existed in more than 2 normal or blood samples included in GTOL and our previously reported organoid libraries (PTOL and CTOL) (Fujii et al., 2016) (Seino et al., 2018). The list of detected SNV and indels after SNP-filtering is shown in Table S3.

To assess genetic stability during passage and to dissect genetic heterogeneity in mixed-type GC organoids, we measured variant allele frequencies (VAFs) using GATK-detected variants with coverage $\geq 100$ which were selected before SNP filtering. For mixed-type GC organoids, GATK-detected variants were SNP-filtered and shown in Table S6.

For copy number analysis, 500 ng of genomic DNA was applied to the CGH/SNP microarray (CytoScan HD, Thermo Fisher Scientific), according to the manufacturer's instructions. We used "apt-copynumber-cyto-ssa" in the Affymetrix Power Tools (version 1.19.0) with normal-diploid-normalization option to obtain probe-level copy number and the allele difference. All parameters were set according to recommendation in user manual. Segmentation analysis was performed with "segmentCGH" function in the R/Bioconductor package "rCGH" (version 1.8.1) using $\log_2$ ratio values of CN-probes. The mean $\log_2$ ratio of segments were visualized after centering the median copy number of each sample. GISTIC2.0 was used to identify recurrent copy number alterations and calculate gene-level copy number. We detected a focal amplification at the tail end of chromosome 14 in all samples, even in normal organoids. We judged this amplification event as a platform-specific artifact, and excluded all probes within the genomic range of chr14:106000000-107349540 from GISTIC2.0 analysis. Gene-level Log2Ratio was thresholded at 1 and $-1$ to detect gene amplification and homozygous deletion.

For methylation analysis, 500 ng of genomic DNA was subjected to bisulfite conversion and applied to an Infinium MethylationEPIC microarray (Illumina) according to the manufacturer's instructions. We used R/Bioconductor package "wateRmelon" (version 1.20.3) to process raw methylation data. Raw methylation data of 35 GC organoids and 15 normal/normal-like organoids were normalized by the dasen function, and outliers were removed by the pfilter function. Probes targeting SNPs and genes located on sex chromosomes were filtered out before analysis. We used K-means clustering (K=3) to determine GC organoid subtypes ($CIMP^+$, $CIMP^-$ and normal/normal-like). Principal component analysis (PCA) was performed using probes exhibiting large variance (M-value variance $> 4$). Gene methylation level was obtained by selecting a probe with the largest negative correlation to the expression in probes mapped to the same gene loci (from 1.5 kbp upstream of the transcription start site to the transcription end site). Methylation levels of top 1,000 genes exhibiting the largest variance across GC organoids were visualized in Figure 1D. Hierarchical clustering was performed with "hclust" function in R using Euclidean distance and ward.D2 linkage metrics. GC33 was excluded from all statistical analyses as it largely shared molecular characteristics with GC34, which was derived from the same patient as GC33.

### Genetic screening for the Ri phenotype

A gene was regarded as "mutated" when it had a homozygous mutation and the mutation resulted in a non-synonymous substitution or splice-site disruption. As an exception, heterozygous mutations in *KRAS*, *RHOA* and *PIK3CA* with known oncogenic impact were regarded as "mutated." Mutated genes identified in less than 2 GC organoids and genes with mutation frequencies less than 10 /Mbp were filtered out. Mutation frequency of each gene in Ri GC organoids was compared to that in WRd GC organoids by Fisher's exact test. 314 genes and all combinations of 2 genes from the 314 genes were examined. GC33 was excluded from the genetic screening due to the reason mentioned above. Mutated genes enriched in Ri GC organoids are shown in Table S4.

### Gene Expression Microarray Analysis

Organoids were cultured from single cells for 5 days in the complete culture condition. RNA was extracted from organoids using the RNeasy Plus Mini Kit (QIAGEN). RNA quality was evaluated based on the RNA Integrity Number (RIN) value determined in RNA6000 assays (Agilent). Only specimens with RIN $> 7.0$ were used in this study. Gene expression profiling was performed using the PrimeView Human Gene Expression Array (Affymetrix) according to the manufacturer's instructions. Raw expression data of 36 GC organoids and 18 normal/normal-like organoids were normalized using the rma function in the R/Bioconductor package

"affy" (version 1.56.0). We detected non-biological batch effects related to the date of experiments, and employed "ComBat" function in R/Bioconductor package "sva" (version 3.26.0) to compensate for the batch effects. Whether each sample was a cancer organoid or normal/normal-like organoid was passed to the ComBat function as a covariate to distinguish batch effects and biologically meaningful gene expression changes. PCA was performed using probesets exhibiting large variance (SD of log2 signal intensity > 1). For integrative gene expression analysis of gastric and colonic organoids, data normalization was conducted independently from the expression analysis of 54 gastric organoids. Gene expression data of 58 colonic organoids were previously reported (Fujii et al., 2016) (GSE74843). Raw expression data of 56 colonic organoids excluding 2 neuroendocrine carcinomas were combined with 54 gastric organoids and normalized as described above. Two covariates, the organoid status (cancerous or not) and the origin (colon or stomach) were used for batch effect compensation. The gene expression data of GC organoids are available in Gene Expression Omnibus (GSE112369).

### Gene expression data analyses

For each gene, $\log_2$ expression value was obtained by selecting a probeset with the largest variance in probesets targeting the same gene. To obtain gene signatures from the designated group of organoids, we determined differentially expressed genes (DEGs) by Welch's t test using $\log_2$ gene expression values. GC33 was excluded from all statistical analyses due to the reason mentioned above. Genes exhibiting small variance ($\log_2$ expression SD < 1.25) were excluded from DEG analysis. False discovery rates (FDR) were calculated by adjusting *p* values using the Benjamini-Hochberg procedure. We determined DEGs with an FDR cutoff of 0.2, and a fold change (FC) cutoff of 2. As an exception, a FC cutoff of 3 was used for DEGs between IM and normal/normal-like organoids. Genes upregulated (or downregulated) in $CIMP^+$ GC organoids compared to both of $CIMP^-$ GC and normal/normal-like organoids were designated as CIMP genes. DEGs between WRi and non-WRi GC organoids were classified into 4 clusters by hierarchical clustering, and then the cluster specifically upregulated in WRi was designated as WRi genes. Hierarchical clustering was performed with "hclust" function in R using Euclidean distance and ward.D2 linkage metric.

### Survival Analysis using Public Database

Raw expression data (.CEL files) of 300 primary GC samples deposited by Cristescu et al. (Cristescu et al., 2015) were downloaded from Gene Expression Omnibus (GEO; GSE62254). Raw expression data were normalized using the rma function in the R/Bioconductor package "affy" (version 1.54.0), and $\log_2$ gene expression was obtained by selecting a probeset with the largest variance in probesets targeting the same gene.

RSEM-normalized expression data (RNA Seq V2 RSEM) of 265 primary GC samples deposited by TCGA (Cancer Genome Atlas Research Network, 2014) were downloaded via cBioPortal. Survival analysis was performed using samples that had both expression data and disease free survival data. WRi gene expression score was determined by "gsva" function in the R/Bioconductor package "GSVA" (version 1.26.0) and was dichotomized at the $90^{th}$ percentile. Survival analysis was performed with the log-rank test.

### Real-Time Quantitative PCR

Total RNA was extracted from tissues using TissueLyser LT (QIAGEN) and the RNeasy Mini Kit (QIAGEN), and cDNA was synthesized using the Omniscript RT Kit (QIAGEN), according to the manufacturers' instructions. Real-time qPCR was performed using Universal Probe Library (UPL) probes and FastStart Essential DNA Probes Master (Roche) on LightCycler 96 device (Roche). Relative gene expression levels were calculated using the delta–delta Ct method.

### Capillary-based Immunoassay

For APC expression analysis, organoids were grown under optimal growth culture conditions. For phospho-ERK-production analysis, organoids were grown under optimal growth culture conditions, followed by cultured without EF for 3 days and with or without 1 μM pan ERBB receptor inhibitor (Merck Millipore). For RHOA expression analysis, organoids were grown under optimal growth culture conditions, followed by cultured with doxycycline (50 ng/ml) for 6 hr. Proteins were extracted from organoids using Cell Lysis Buffer (#9803, CST) according to the manufacturer's instructions. Protein separation and detection were performed using an automated capillary electrophoresis system (Simple Western system and Compass software; proteinsimple). Wes Separation Capillary Cartridges for 66-440 kDa and 12-230 kDa were used for APC and the other proteins, respectively. Antibodies against the following proteins were used; ERK-1/2 (#9102, CST, 1:50), phospho ERK1/2 (T202/Y204) (#4370, CST, 1:50), APC (#2504, CST, 1:50), RHOA (#2117S, CST, 1:50) and anti-β actin (#A1978, Sigma, 1:50). Signals were detected with an HRP-conjugated secondary anti-rabbit antibody and were visualized using proteinsimple software.

### Flow cytometry analysis

Cell surface expression of Frizzled receptors was analyzed using flow cytometry using a WRd GC organoid line (GC13), an RZ-mutated line (GC16) and a CT-mutated line (GC31). Four to five days prior to analysis, organoids were passaged by single cell dissociation and maintained in a WR-including culture condition. The organoids were Wnt/R-spondin-starved for 24 hr and then cultured with or without R-spondin for 16 hr. For cell labeling, organoids were dissociated using enzyme-free PBS-based dissociation buffer (13151014, Thermo Fisher Scientific) and incubated for 15 min at room temperature in PBS containing 0.1% (v/v) bovine serum albumin (BSA) and an anti-pan Frizzled monoclonal antibody (TAB-880, Creative Biolabs). Cell suspension was washed twice

with PBS by centrifuging, and the cell palettes were suspended in PBS containing 0.1% BSA and a phycoerythrin (PE)-conjugated goat anti-human IgG Fcγ fragment-specific antibody and incubated for 15 min at room temperature. The cells were washed again twice with PBS, suspended in PBS containing DAPI (564907, BD Biosciences, 1:1000), and analyzed using a cell sorter (SH800, Sony). For control, cells were labeled only with the secondary antibody.

### Xenografting of GC organoids

Prior to the assay, the organoids were labeled by electroporation with a GFP-puro PiggyBac vector (System Biosciences) as previously described (Matano et al., 2015). In parallel, we prepared fibroblasts from a HIO (kindly provided from James Wells, Cincinnati Children's Hospital). After the isolation by manual picking, HIOFs were expanded in the HFDM-1 medium (Cell Science & Technology) supplemented with 5% FBS and 1% penicillin/streptomycin, cryopreserved at early passages, and recovered 1 week before the transplantation. For xenografting, GC organoids were isoloated from Matrigel using Cell Recovery Solution (BD Biosciences) and physically dissociated into cell clusters by brief pipetting. For each transplantation, GC cell clusters (equivalent to $1 \times 10^5$ cells) and detached HIOFs ($2 \times 10^5$ cells) were re-suspended in 10 μL of cold Matrigel and injected into a kidney subcapsule of a NOG mouse (8-12 weeks old, male). Each GC organoid line was transplanted into 4 independent NOG mice.

At 2 months post-transplantation, mice were euthanized and the grafts were isolated. Tumor sizes were measured as the areas of GFP fluorescence (Nikon Multi-zoom microscopy, LuminaVision software). The grafts were fixed for subsequent histological analyses. For Porcn-i-treatment experiments, tumor-bearing mice were randomized before treatment and treated with C59 (50 mg/kg, administered daily by oral gavage) as demonstrated in Figure 7D.

### Immunohistochemistry and *in situ* hybridization

Isolated xenografts were immediately fixed with 4% paraformaldehyde. The standard protocols for sectioning paraffin-embedded tissues and H&E staining were used. Whole-mount immunofluorescent staining of organoids was performed as previously described (Seino et al., 2018). For immunostaining, rat anti-integrin-α6 (313601, Biolegend, 1:100), rabbit anti-α-catenin (CTNNA1) (C2081, Sigma-Aldrich, 1:2000), rabbit anti-Ki67 (ab16667, abcam, 1:100), mouse anti-CDX2 (MU392, BioGenex, 1:300) and goat anti-E-cadherin (AF748, R&D, 1:100) antibodies were used, with subsequent labeling by Alexa Fluor 488-, 568- or 647- conjugated anti-rat, -goat, -rabbit or -mouse antibodies (Thermo Fisher Scientific). Alexa Fluor 647-phalloidin (A22287, Thermo Fisher Scientific) was used for the visualization of F-actin. Nuclei were counterstained with Hoechst 33342 (Thermo Fisher Scientific). For *in situ* hybridization, we used an RNAscope 2.5 HD Kit (Advanced Cell Diagnostics), according to the manufacturer's instructions. Probes for *AXIN2* and *EBER1* were designed by Advanced Cell Diagnostics. *PPIB* and *DapB* genes were used as positive and negative controls, respectively. Images were captured using a BZ-X710 digital microscope (Keyence) or a confocal microscope (SP8, Leica).

## QUANTIFICATION AND STATISTICAL ANALYSIS

Pairwise analyses for tumor volumes and gene expression values were performed using unpaired two-tailed Welch's t test. For further statistical details, refer to each figure legend.

## DATA AND SOFTWARE AVAILABILITY

The accession number for the gene expression microarray data reported in this paper is GEO: GSE112369.

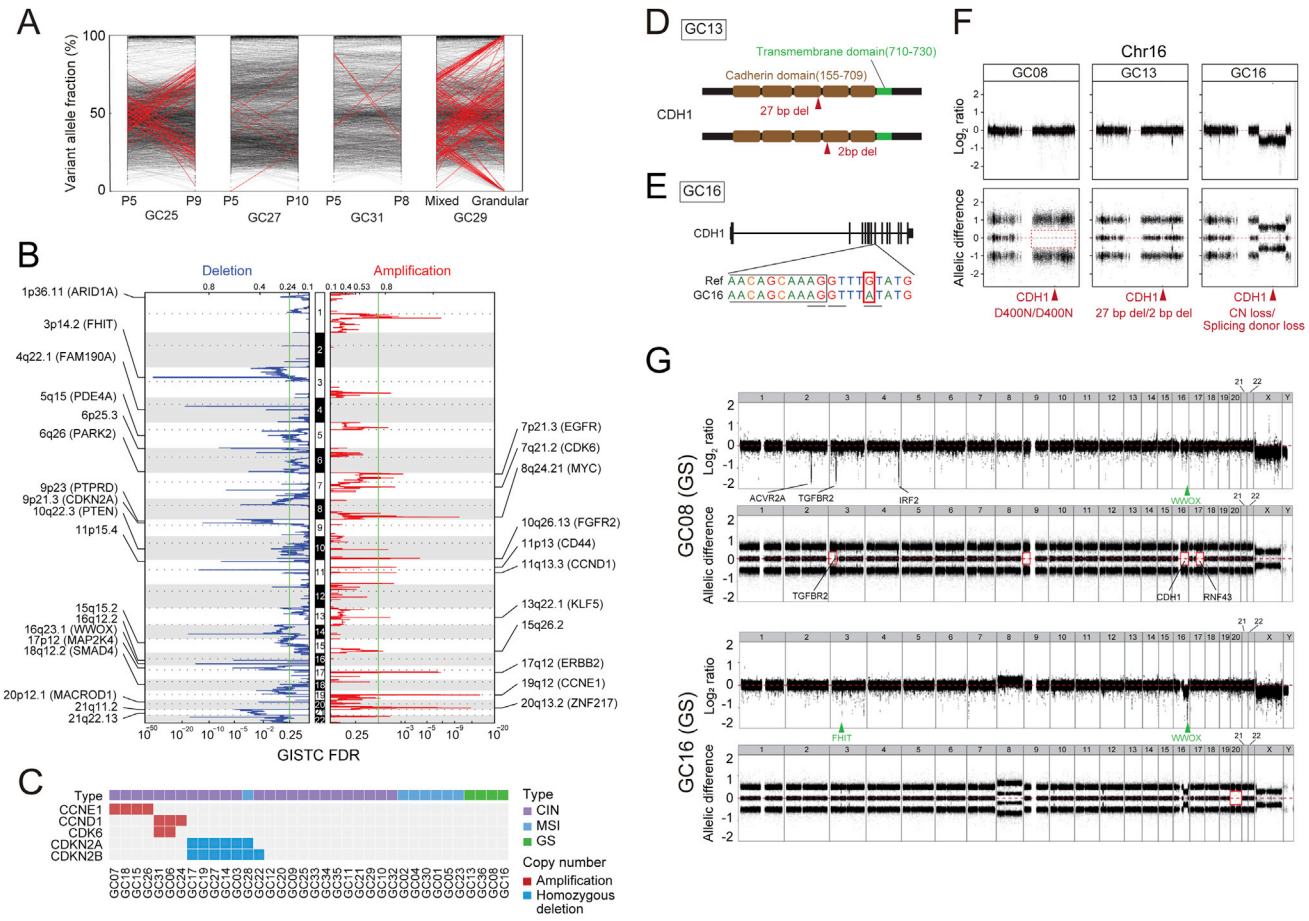


**Figure S1. Molecular Analyses of the GTOL, Related to Figure 1**

(A) Alteration of variant allele fractions of CIN-GC organoids (GC25, 27, 31) during culture. Dots represents SNVs and indels detected by whole-exome sequencing with coverage ≥ 100 reads, and connected with lines between early and late passage. Passage numbers are shown on the bottom. Red lines indicate the mutations with variant allele frequency changes ≥ 25%. Drastic change in variant allele fractions was observed after the clonal isolation of GC29 (far right). A glandular clone was isolated from a mixed subtype of GC organoids (see also Figure 2 and Figure S3 for the morphological criteria).

(B) GISTIC plots show significantly recurring focal deletions (left) and amplifications (right). Annotated peaks with FDR < 0.25 are shown.

(C) Focal amplification of *CCNE1*, *CCND1* and *CDK6* and focal deletions of *CDKN2A/2B* were mutually exclusive in the GTOL. Colors for molecular subtypes and copy number statuses are denoted on the right.

(D and E) Representative images depicting somatic *CDH1* mutations in GS-GC organoids, GC13 (D) and GC16 (E). GC16 had a focal deletion accompanied by a point mutation at the consensus splicing site (underbars) of the remaining allele.

(F) *CDH1* gene alterations in GS-GC organoids. Chromosomal statuses of the region covering *CDH1* are visualized by copy numbers (top) and zygosity (bottom). GC08 has a CN-LOH.

(G) Whole genome chromosomal statuses of 2 GS-GC organoid lines. Copy number changes are shown on top, and allele frequencies are shown on bottom. Red rectangles denote CN-LOH. Genetic mutations/deletions are superimposed on the locus. Green arrow heads indicate fragile-site genes.

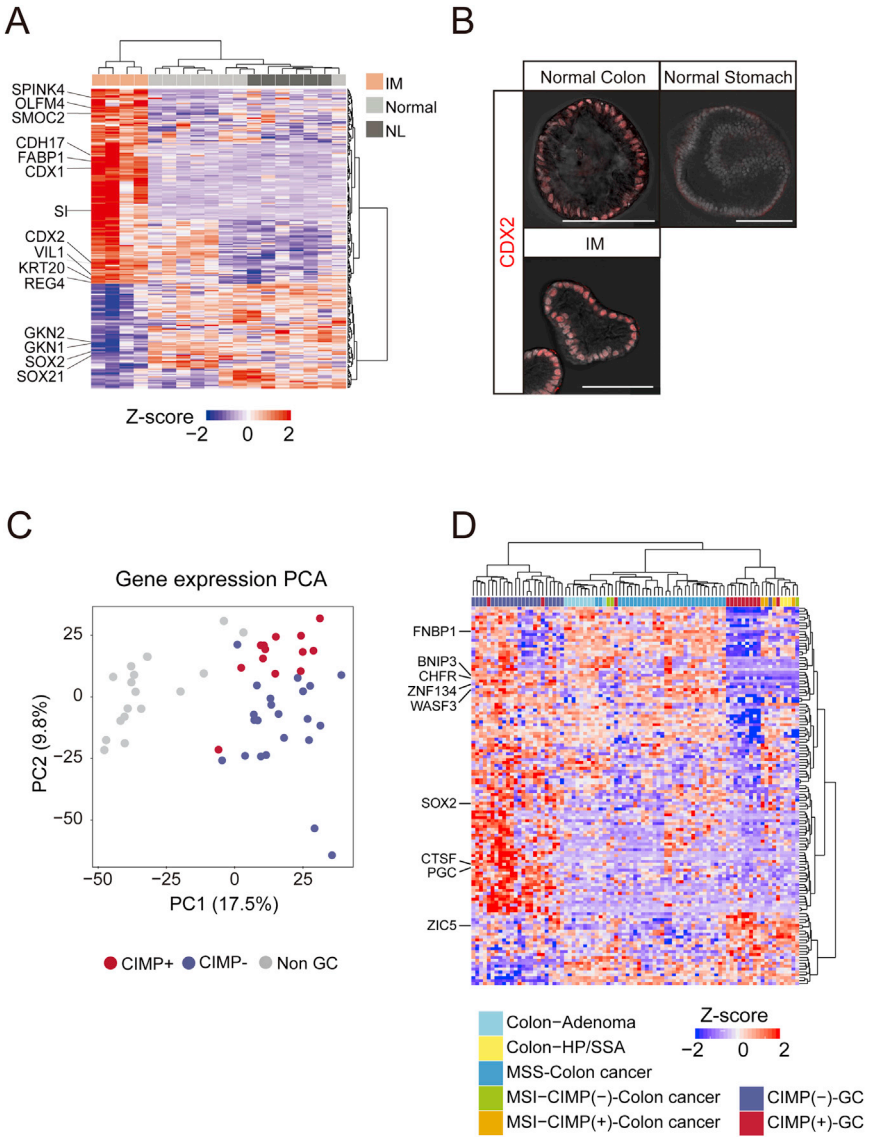


**Figure S2. Gene Expression Analyses of Gastric Organoids, Related to Figure 1**

(A) The expression of differentially expressed genes between normal/NL and IM organoids.

(B) CDX2 immunostaining in colonic normal organoids (top left), gastric normal organoids (top right) and IM organoids (bottom). Nuclear counterstaining, Hoechst 33342. Scale bar, 100 μm.

(C) PCA plots of the transcriptome of the GTOL annotated with the CIMP status of GC organoids. Non-GC organoids are shown in gray.

(D) Hierarchical clustering of GC and colorectal tumor organoids based on the expression of CIMP genes. Color annotation for each organoid subtype is shown on bottom. $CIMP^{+}$ GC organoids, and $CIMP^{+}$ colorectal tumor organoids cluster together.

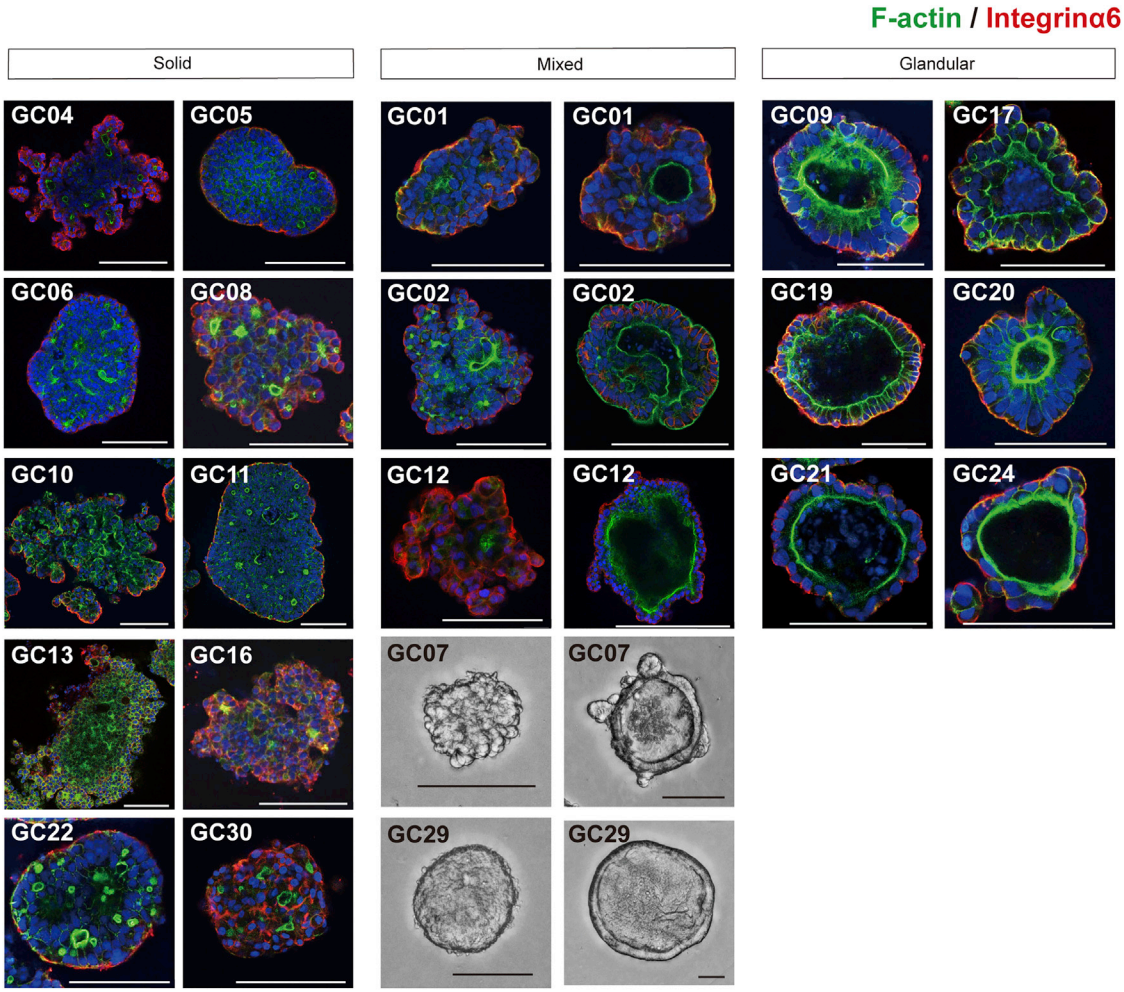


**Figure S3. Morphological Characterization of GC Organoids, Related to Figure 2**

Images of GC organoids with the indicated morphological subtypes. Confocal images depict the apicobasal polarity of organoids with F-actin (green) and integrin α6 (red) staining. For mixed subtype GC organoids, organoid subpopulations with solid (left) and glandular (right) morphologies are demonstrated. Bright-field images are shown for GC07 and GC29. Scale bar, 100 μm. Nuclear counterstaining, Hoechst 33342.

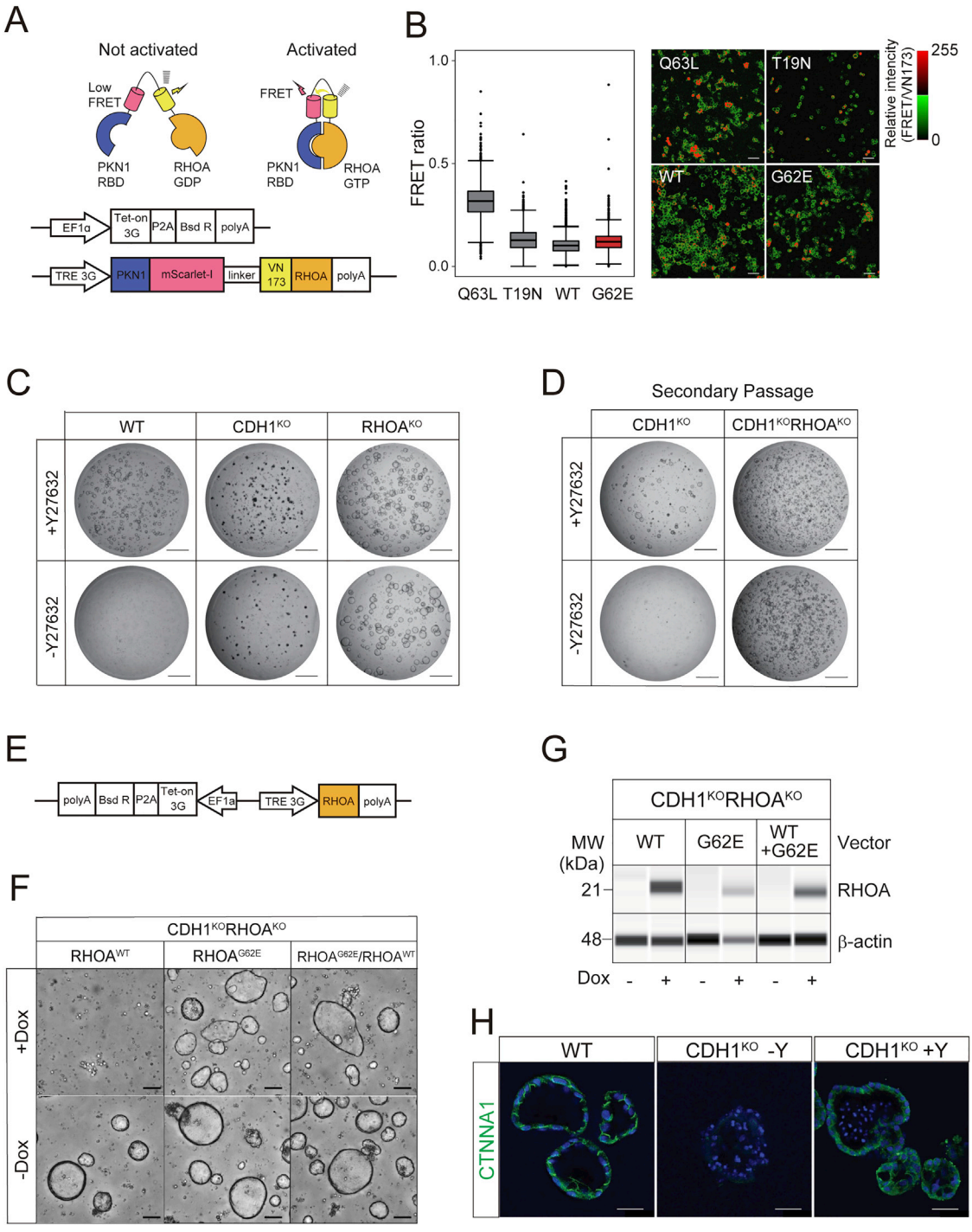


**Figure S4. Genetic Engineering of Adhesion-Associated Genes in Gastric Organoids, Related to Figure 2**

(A) Schematics depicting the structure and vector constructs of the RHOA FRET biosensor.

(B) FRET intensities of biosensors with mutant or WT RHOA. Mutant RHOA$^{G62E}$ shows low affinity to a consensus RHOA binding domain. Scale bar, 50 μm.

(C) Colony formation of WT, *CDH1*$^{KO}$, *RHOA*$^{KO}$ gastric organoids after single cell dissociation cultured with (top) or without a ROCK inhibitor (Y-27632) (bottom). Albeit with reduced efficiency, *CDH1*$^{KO}$ and *RHOA*$^{KO}$ cells are capable of forming organoids without ROCK inhibition. Scale bar, 1 mm.

(D) The images of *CDH1*$^{KO}$ and *CDH1*/*RHOA* DKO gastric organoids in passage 2. After each passage, organoids were treated with (top) or without Y-27632 for 2 days (bottom). Only *CDH1*/*RHOA*-DKO organoids propagated after the secondary passage. Scale bar, 1 mm.

(E) Vector constructs for expressing doxycycline-inducible wild-type or mutant RHOA.

*(legend continued on next page)*

(F) Wild-type RHOA and/or G62E mutant RHOA was induced into *CDH1*/*RHOA* DKO gastric organoids. Expression of mutant $RHOA^{G62E}$ did not change the cystic structure of *CDH1*/*RHOA* DKO gastric organoids. Scale bar, 100 μm.

(G) Capillary-based immunoassays for Dox-induced RHOA expression. Loading control, β-actin.

(H) Immunohistological images of CTNNA1 (green) in normal gastric organoids maintained in a standard culture condition (left), $CDH1^{KO}$ organoids cultured without a ROCK-inhibitor (middle) and with a ROCK inhibitor (right). Scale bar, 100 μm.

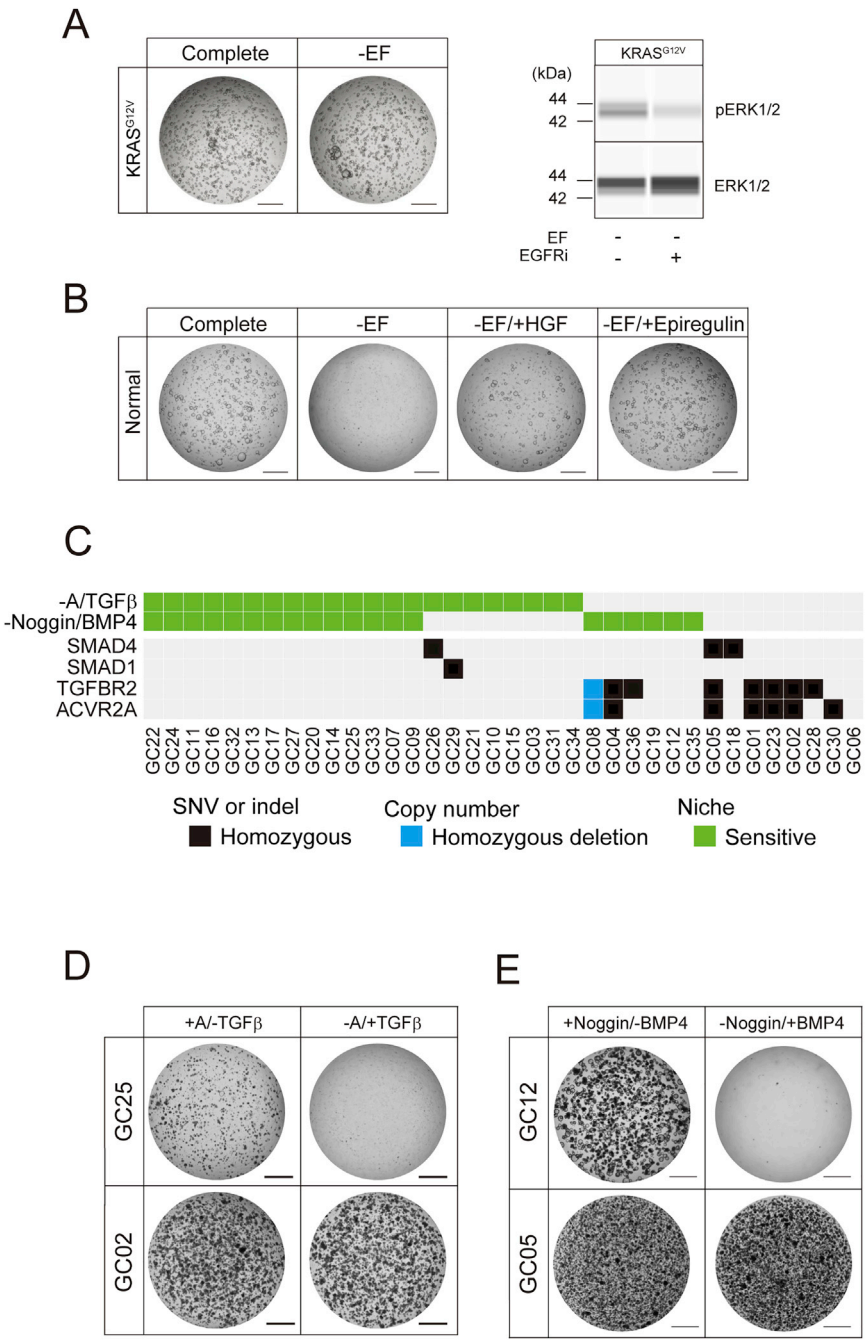


**Figure S5. Genetic Alterations Regulating EGF/FGF10 or BMP/TGF-β Niche Dependency, Related to Figure 3**

(A) KRAS$^{G12V}$ knocked-in gastric organoids grew in the absence of EF (left) and show ERK phosphorylation, which is partially decreased by Ei treatment (right).

(B) Normal gastric organoids failed to grow without EF. HGF or epiregulin substitutes for the EF niche in normal gastric organoids.

(C) Dependencies of GC organoids on a TGF-β inhibitor and Noggin in association with *SMAD4*, *SMAD1*, *TGFBR2* and *ACVR2A* gene alterations. For each condition, organoids were treated with TGF-β (5 ng/ml) and BMP4 (100 ng/ml) in the absence of a TGF-β inhibitor (-A) and Noggin, respectively. Organoid lines sensitive to the corresponding treatments were colored in green. Further color and graphical specifications are demonstrated on the bottom.

(D) Representative images of TGF-β–sensitive (top) and -resistant GC organoids (bottom) treated with the indicated conditions.

(E) Representative images of BMP4-sensitive (top) and resistant GC organoids (bottom) treated with the indicated conditions. Scale bar, 1mm.

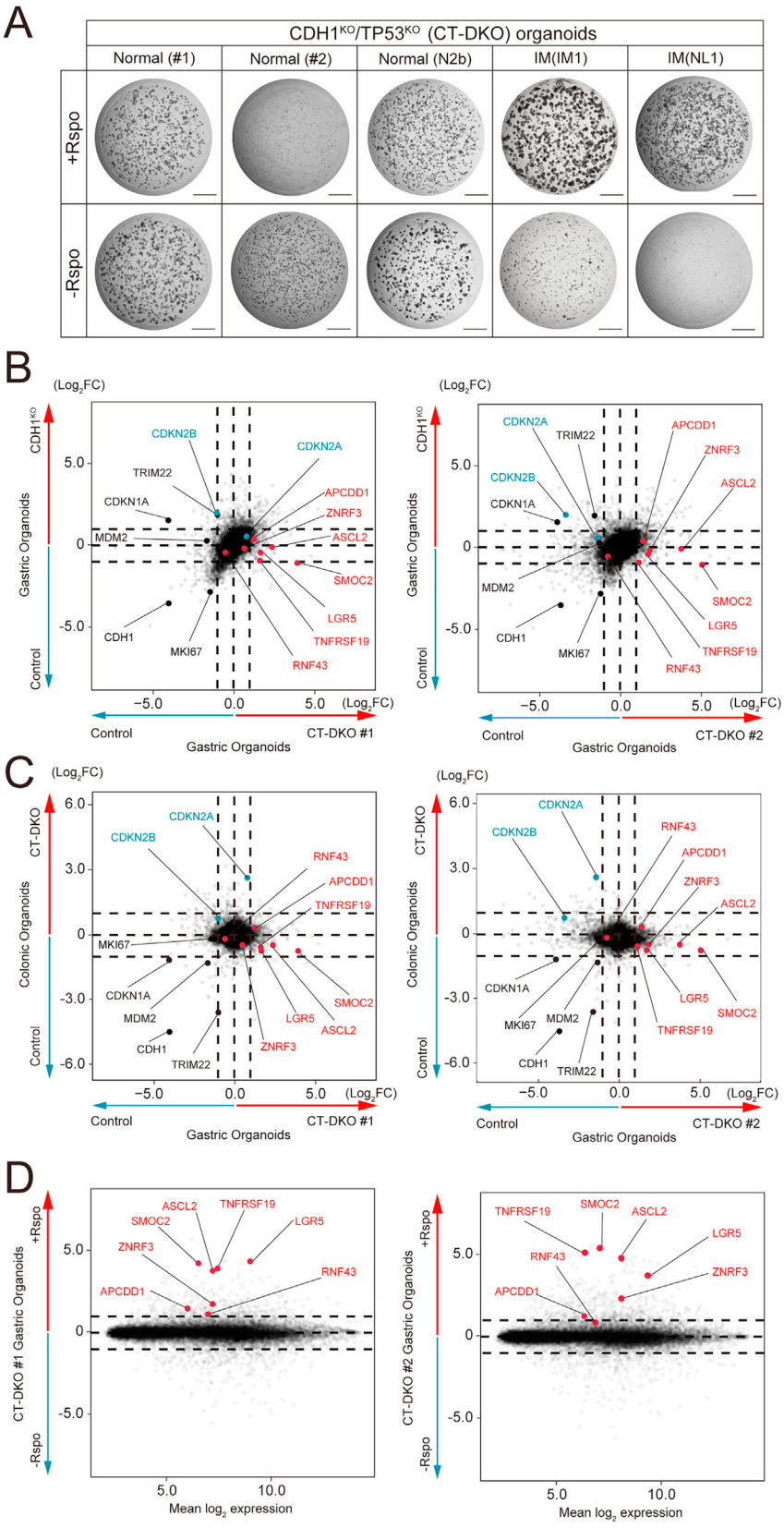


*(legend on next page)*

**Figure S6. Characterization of *CDH1/TP53* Double KO Organoids, Related to Figure 6**

(A) Images of *CDH1/TP53*-DKO normal and IM gastric organoids cultured with (top) or without (down) R-spondin. *CDH1/TP53* DKO conferred R-spondin-independent growth capacity on normal gastric organoids (N1 subclones and N2b) but not on IM organoids (IM1 and NL1). Scale bar, 1 mm.

(B) Transcriptome change by *CDH1* single KO or *CDH1/TP53* DKO in gastric organoids. Each dot shows a relative gene expression in *CDH1* single KO (y-axes) or *CDH1/TP53* DKO (x-axes) gastric organoids versus normal gastric organoids. Data from two *CDH1/TP53* DKO gastric organoid subclones was used. Wnt target genes and cell cycle inhibitors were highlighted in red and blue, respectively.

(C) Comparison of *CDH1/TP53* DKO gastric and colon organoids. Y-axes show gene expression change in colon organoids and x-axes show gene expression change in gastric organoids by *CDH1/TP53* DKO.

(D) MA plots of *CDH1/TP53* DKO gastric organoids cultured in the presence or absence of R-spondin. Both subclones show intact Wnt target gene upregulation by treatment with R-spondin. Dotted lines show $\log_2$(fold change) = 0 or ±1.

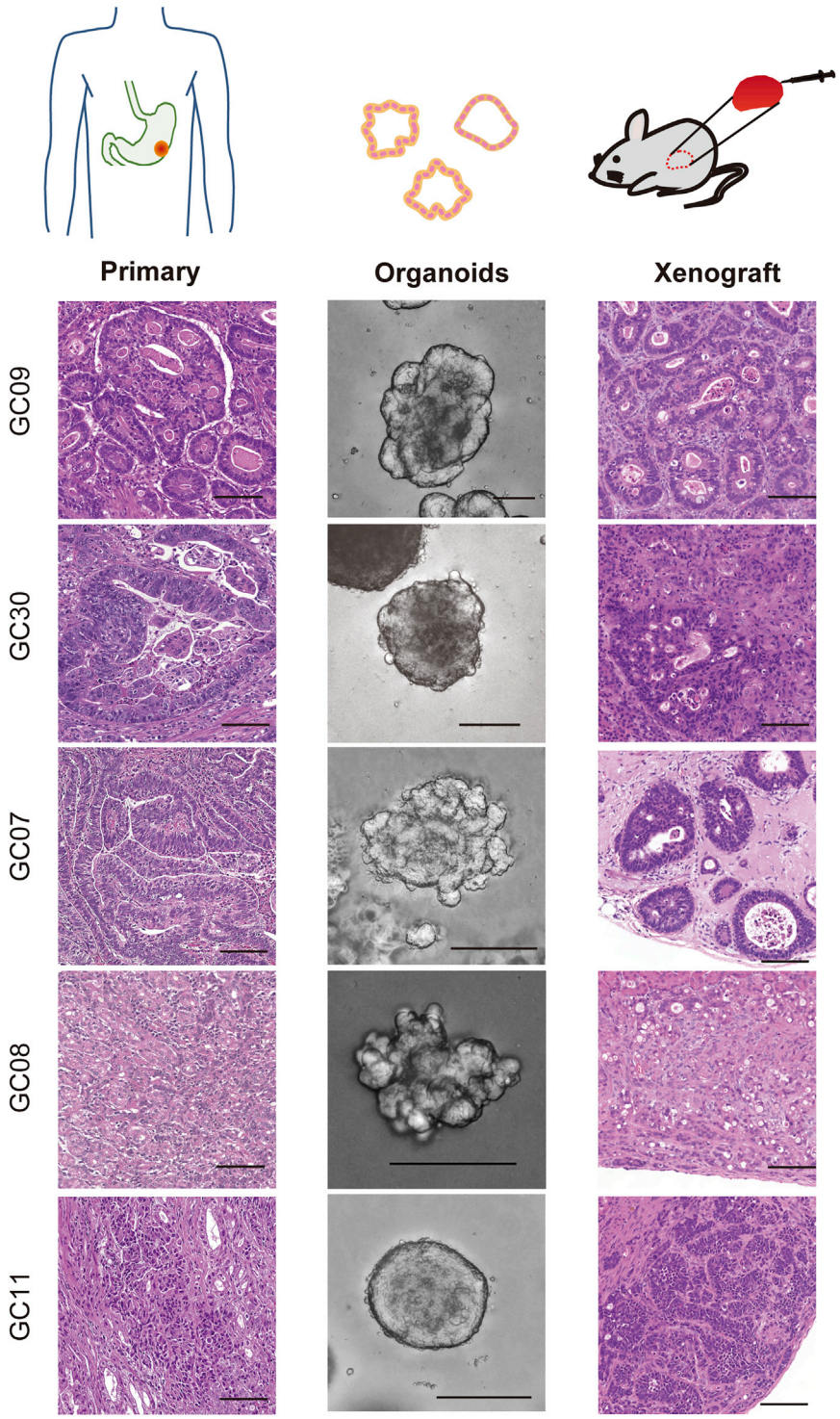


**Figure S7. Morphological Recapitulation of the Parental Pathology in Organoids and Xenografts, Related to Figure 7**

Representative images of the parental tumor histology (left), organoids (middle) and the xenograft histology (right). The ID of each GC organoid is on the left. In all cases, original histological identities were preserved during culture and after xenografting. Scale bar, 100 μm.